FEBRUARY 26 2026

Impact of species diffusion on the attenuation of acoustic waves in multi-component planetary atmospheres

Benedict Piñeyro ; Roberto Sabatini ; Jonathan B. Snively

J. Acoust. Soc. Am. 159, 1721–1748 (2026)
https://doi.org/10.1121/10.0042249

JASA ARTICLE

Impact of species diffusion on the attenuation of acoustic waves in multi-component planetary atmospheres

Benedict Piñeyro,[1,a),b)] Roberto Sabatini,[2,c)] and Jonathan B. Snively[1,d)]
[1]*Physical Sciences Department and Center for Space and Atmospheric Research, Embry-Riddle Aeronautical University, USA*
[2]*Ecole Centrale de Lyon, CNRS, Universite Claude Bernard Lyon 1, INSA Lyon, LMFA, UMR5509, 69130, Ecully, France*

ABSTRACT:
Acoustic waves in planetary atmospheres are attenuated by dissipative processes such as viscous stresses and heat conduction, particularly in the rarefied upper layers where multiple species exist in diffusive equilibrium. While the roles of viscosity and thermal conduction in wave attenuation are well understood, species diffusion—the relative motion of molecular species different from the bulk gas driven by gradients in concentration, pressure, and temperature—has received less attention. This study investigates species diffusion as an additional attenuation mechanism in dilute, multi-component gas mixtures, using generalized macroscopic transport equations derived from kinetic theory that reduce to the classical Navier–Stokes equations in the single-species limit. Using a multiple-scales approach, we derive a dispersion relation for linear acoustic and gravity waves, from which an expression for attenuation in multi-species atmospheres is obtained. We apply this framework to the upper atmospheres of Earth, Venus, Mars, Titan, Uranus, and Neptune. Results show that species diffusion—primarily via barodiffusion (diffusion driven by pressure gradients)—can significantly enhance acoustic attenuation on Earth, Venus, and Mars, reaching up to 16%, 45%, and 17%, respectively. On Earth, the effect is most pronounced above 150 km, where light and heavy species such as molecular nitrogen and atomic oxygen coexist in appreciable concentrations. In contrast, species diffusion plays a minor role—contributing less than $\leq 5\%$—on Titan, Uranus, and Neptune, with bulk and shear viscosity effects dominating wave attenuation in these atmospheres. These findings expand existing models of planetary wave propagation and have implications for planetary diagnostics, remote sensing, and space missions.
 https://doi.org/10.1121/10.0042249

(Received 21 July 2025; revised 25 December 2025; accepted 1 January 2026; published online 26 February 2026)

[Editor: Andi Petculescu] Pages: 1721–1748

NOMENCLATURE

$C_{kl}, k, l \in S$	Multi-component flux diffusion coefficients
c	Speed of sound
c_p	Constant-pressure specific heat
c_{pk}	Constant-pressure specific heat of the kth species
c_v	Constant-volume specific heat
c_{vk}	Constant-volume specific heat of the kth species
e	Internal energy per unit mass or specific internal energy
e_k	Internal energy per unit mass or specific internal energy of the kth species
e_t	Total energy per unit mass or specific total energy
$\boldsymbol{\mathcal{F}}_k$	Diffusion flux vector of the kth species
$\boldsymbol{g}$	Gravitational acceleration vector
$\mathfrak{h}_k$	Enthalpy per unit mass or specific enthalpy of the kth species
$\mathfrak{h}$	Enthalpy per unit mass or specific enthalpy
k_B	Boltzmann constant
M	Molar mass
m	Mass
N_A	Avogadro constant
N_{dof}	Number of Degrees of Freedom
n_s	Number of species in the mixture
p	Pressure
$\boldsymbol{\mathcal{Q}}$	Heat flux vector
R	Universal gas constant
$S = 1, \ldots, n_s$	Set of species indices
T	Temperature
$\mathbb{T}$	Viscous stress tensor
$\boldsymbol{v}$	Hydrodynamic or mass average velocity vector
X_k	Mole fraction of species k
Y_k	Mass fraction of species k
γ	Specific heat ratio
λ	Thermal conductivity
μ_b	Bulk viscosity
μ	Shear viscosity
$\mathcal{V}_k$	Diffusion velocity vector of the kth species
$\xi_k, k \in S$	Rescaled thermal diffusion ratios
ρ	Density of the mixture
ρ_k	Density of the kth species

[a)]Email: pineyrob@erau.edu
[b)]Now at: School of Earth and Space Exploration, Arizona State University, Tempe, AZ 85287, USA. Email: bpineyro@asu.edu
[c)]Email: roberto.sabatini@ec-lyon.fr
[d)]Email: snivelyj@erau.edu

I. INTRODUCTION

The study of acoustic, particularly infrasonic, and acoustic-gravity wave propagation in planetary atmospheres has gained considerable attention over recent decades owing to its wide-ranging relevance in geophysics and remote sensing (Bradley, 2007; Brown and Hall, 1978; Le Pichon *et al.*, 2009). Critical applications include: (1) detection, localization, and characterization of both geophysical and anthropogenic sources of infrasonic signals (Bowman *et al.*, 2022; Garcia *et al.*, 2022; Inchin *et al.*, 2020; Le Pichon *et al.*, 2009; Matoza *et al.*, 2022; Nozuka *et al.*, 2024; Sabatini *et al.*, 2016b; Sabatini *et al.*, 2019; Watson *et al.*, 2022; Zettergren and Snively, 2015); (2) acoustic reconstruction of atmospheric properties, such as sound speed and wind profiles along propagation paths (Averbuch *et al.*, 2020; Blixt *et al.*, 2019; Chunchuzov *et al.*, 2015; Lalande *et al.*, 2012; Park *et al.*, 2022; Vera Rodriguez *et al.*, 2020; Vorobeva *et al.*, 2023); (3) investigations into wave propagation, dissipation, and energy dynamics in Earth's upper atmosphere (Fritts and Alexander, 2003; Heale *et al.*, 2018; Walterscheid and Hickey, 2001; Hickey *et al.*, 2011; Vadas, 2013); and (4) exploring wave-induced phenomena in planetary atmospheres, including seismoacoustic coupling and radiative damping (Averbuch *et al.*, 2023; Chide *et al.*, 2024; Eckermann *et al.*, 2011; Froment *et al.*, 2024; Gerier *et al.*, 2024; Hickey *et al.*, 2000; Martire *et al.*, 2020; Petculescu, 2016). These applications require comprehensive theoretical and computational frameworks, alongside measurements of source-induced disturbances, to understand the evolution of acoustic and gravity waves as they traverse atmospheric layers.

Transport phenomena strongly influence acoustic and gravity wave propagation by driving the microscopic redistribution of mass, momentum, and kinetic energy. These include mass transport due to diffusion, momentum transport induced by viscous stresses, and kinetic energy transport via heat conduction. Such mechanisms cause wave attenuation and dispersion (Bass *et al.*, 1984; Bauer, 1972; Fedorenko *et al.*, 2021; Godin, 2014; Pitteway and Hines, 1963; Richmond, 1978; Sutherland and Bass, 2004), effects that become more pronounced in rarefied regions like Earth's thermosphere (Heale *et al.*, 2014; Sabatini *et al.*, 2016a). Additionally, in molecular gases with internal degrees of freedom, relaxation phenomena constitute another relevant mechanism contributing to wave attenuation and dispersion (Bass *et al.*, 1984; Bauer, 1972; Hines, 1977a,b; Pierce, 1978; Sutherland and Bass, 2004).

Research on acoustic wave attenuation has a long history, with notable developments dating back to the mid-19th century. The classical theory of acoustic wave absorption was initiated by Stokes (2009), who derived an expression for attenuation due to viscosity in a monoatomic gas. Kirchhoff (1868) later extended this theory to incorporate thermal conductivity effects, establishing the foundation for the modern understanding of sound attenuation caused by thermoviscous phenomena–commonly referred to as classical absorption of acoustic waves (Bass *et al.*, 1984; Garrett, 2020). Subsequent progress, particularly in the context of Earth's atmosphere, expanded the classical absorption model to include vibrational relaxation effects (Bass *et al.*, 1984; Bauer, 1972; Markham *et al.*, 1951; Pierce, 1978; Sutherland and Bass, 2004). These advances have formed the basis for many acoustic wave attenuation models applied in planetary acoustics studies (Garcia *et al.*, 2017; Bass and Chambers, 2001; Gillier *et al.*, 2024; Petculescu and Lueptow, 2007; Petculescu, 2016; Trahan and Petculescu, 2020).

Most studies on acoustic and gravity wave attenuation have modeled Earth's atmosphere as a single-component gas, an approximation reasonably accurate below approximately 100 km altitude. There, air predominantly consists of a binary mixture of molecular nitrogen (N_2) and molecular oxygen (O_2). Since N_2 and O_2 have similar molecular properties, the atmosphere's multi-component nature has a negligible impact on wave attenuation at these altitudes. Using an expression originally derived by Kohler (1941), studies by Bauer (1972), Bass *et al.* (1984), and Sutherland and Bass (2004) showed that the spatial attenuation rate of acoustic waves due to N_2–O_2 diffusion is less than 1% of the attenuation caused by classical absorption mechanisms. However, above 100 km, Earth's atmosphere transitions into a ternary mixture of N_2, O_2, and atomic oxygen (O) (Walterscheid and Hickey, 2001, 2012). In this rarefied region, species diffusion can become a significant factor influencing wave propagation. To date, only provisional investigations into gravity-wave attenuation in this regime have been conducted. For instance, Hickey *et al.* (2015) examined how species decoupling caused by infrequent collisions–leading to individual species having their own temperatures and velocities–and mutual diffusion influence wave dynamics and dissipation at high altitudes.

Linear theory has provided the basis for deriving dispersion relations and analyzing acoustic and gravity wave propagation through planetary atmospheres (Fedorenko *et al.*, 2021; Godin, 2014; Hines, 1960; Pitteway and Hines, 1963; Vadas and Fritts, 2005; Vadas and Nicolls, 2012). Early studies primarily examined wave propagation in idealized, dissipationless, isothermal, single-component atmospheres. In such cases, the linearized hydrodynamics equations can be reformulated, using a density scaling (Bergmann, 1946; Hines, 1960), into a system with constant coefficients. This reformulation allows harmonic plane wave solutions from which dispersion relations can be derived. However, in realistic dissipative, windy, and non-isothermal atmospheres—where density, pressure, temperature, viscosity, and thermal conductivity vary with altitude—analytical approaches become significantly more challenging. Even with density scaling, the governing hydrodynamic equations cannot be reduced to a system with constant coefficients, rendering plane wave solutions generally inapplicable. Under these conditions, dispersion relations can only be obtained through a local approximation assuming atmospheric properties change gradually over spatial scales comparable to the wavelengths of interest. At such scales, the atmosphere can be locally approximated as homogeneous, allowing local

https://doi.org/10.1121/10.0042249

plane wave solutions. Local dispersion relations for acoustic and gravity waves, incorporating viscous stresses and thermal conduction effects, have been derived and analyzed previously (Godin, 2014; Vadas and Fritts, 2005; Vadas and Nicolls, 2012), but have yet to be extended to multi-component and mutually diffusive gas mixtures.

This work investigates the effects of transport phenomena, particularly species diffusion, on the linear propagation of acoustic and gravity waves in multi-component planetary atmospheres. The atmosphere is modeled as a non-reactive, dilute mixture of atomic and polyatomic ideal gases, with dynamics governed by a set of generalized macroscopic transport equations derived from kinetic theory (Chapman and Cowling, 1939; Ern and Giovangigli, 1994). These include species mass conservation, total mass conservation, momentum, and total energy equations, collectively referred to as the multi-component Navier–Stokes equations. In the limiting case of a single-component gas, the system reduces to the classical Navier–Stokes equations (Landau and Lifshitz, 1987). Special attention is given to the acoustic limit, where a generalized expression is derived for the spatial attenuation rate of low-frequency acoustic waves incorporating viscous stresses, thermal conductivity, and species diffusion. The formulation introduces a closed-form expression for species diffusion in multi-component gas mixtures, extending classical thermoviscous theory to account for interspecies transport. The resulting relation is used to analyze acoustic wave attenuation in Earth's thermosphere and the upper atmospheres of Venus, Mars, Titan, Uranus, and Neptune.

To contextualize species diffusion's contribution, vibrational relaxation—a dominant attenuation mechanism in the lower atmosphere—is included separately using an empirical model (Garcia *et al.*, 2017; Bass and Chambers, 2001; Gillier *et al.*, 2024; Petculescu and Lueptow, 2007; Sabatini *et al.*, 2016a; Sutherland and Bass, 2004; Trahan and Petculescu, 2020). Since attenuation mechanisms are additive (Bass *et al.*, 1984; Bauer, 1972; Evans and Sutherland, 1971), vibrational relaxation can be incorporated without altering the transport framework. The analysis reveals that vibrational relaxation governs wave attenuation below approximately 120 km, while species diffusion becomes increasingly significant above 150 km, where classical thermoviscous mechanisms typically dominate. Recognizing this separation allows for a more accurate assessment of species diffusion's role across different atmospheric layers.

The paper is organized as follows: Sec. II introduces the governing equations for multi-component ideal gas mixtures, following Ern and Giovangigli (1994). Section III derives a generalized dispersion relation for acoustic and gravity waves incorporating species diffusion, with emphasis on the acoustic attenuation coefficient. Section IV presents and discusses results for wave attenuation in Earth's thermosphere and in the atmospheres of Mars and Venus, providing a comparative overview for Titan, Uranus, and Neptune. Detailed results for these outer planetary atmospheres are given in Appendix B. Concluding remarks are presented in Section V.

II. GOVERNING EQUATIONS

A planetary atmosphere is treated as a non-reactive dilute mixture of n_s atomic and polyatomic ideal gases. Its dynamics are assumed to be described by a set of generalized macroscopic transport equations derived from the kinetic theory of gases (Arnault and Guisset, 2022; Chapman and Cowling, 1939; Ern and Giovangigli, 1994), namely, the species mass density equation, the momentum equation, and the total energy equation. These balance equations, as reported by Ern and Giovangigli (1994), are

$$\frac{\partial(\rho Y_k)}{\partial t} + \operatorname{div}(\rho Y_k \boldsymbol{v}) = -\operatorname{div}(\boldsymbol{\mathcal{F}}_k), \quad k \in S, \tag{1a}$$

$$\frac{\partial(\rho \boldsymbol{v})}{\partial t} + \operatorname{div}(\rho \boldsymbol{v} \otimes \boldsymbol{v} + p\mathbb{I}) - \rho \boldsymbol{g} = -\operatorname{div}(\mathbb{T}), \tag{1b}$$

$$\frac{\partial(\rho e_t)}{\partial t} + \operatorname{div}((\rho e_t + p)\boldsymbol{v}) - \rho \boldsymbol{g} \cdot \boldsymbol{v} = -\operatorname{div}(\boldsymbol{\mathcal{Q}} + \mathbb{T}\boldsymbol{v}), \tag{1c}$$

where $S = \{1, \ldots, n_s\}$ is the set of species indices, ρ is the total mass density, $Y_k = \rho_k/\rho$ is the mass fraction of the kth species, i.e., the ratio between the mass density of the kth species ρ_k and the total mass density ρ, $\boldsymbol{v}$ is the hydrodynamic or mass average velocity vector, $\boldsymbol{\mathcal{F}}_k$ is the diffusion flux vector of the kth species, p is the thermodynamic pressure, $\mathbb{I}$ is the identity tensor, $\mathbb{T}$ is the viscous stress tensor, $\boldsymbol{g}$ is the gravitational acceleration vector, $e_t = (e + \|\boldsymbol{v}\|^2/2)$ is the specific total energy with e the specific internal energy and $\|\boldsymbol{v}\|^2/2$ the specific kinetic energy, and $\boldsymbol{\mathcal{Q}}$ is the heat flux vector. The variables $\boldsymbol{\mathcal{F}}_k, \mathbb{T}$, and $\boldsymbol{\mathcal{Q}}$ are referred to as transport fluxes because they represent the molecular transport of mass, linear momentum, and kinetic energy through the gas, respectively.

Equations (1a)–(1c) form the multi-component Navier–Stokes equations, which describe the evolution of mass, momentum, and energy in a mixture of gases, governing the macroscopic dynamics of a dilute multi-component gas mixture. This system generalizes the classical Navier–Stokes equations by incorporating species mass conservation equations that account for diffusive transport of individual gas constituents.

By definition, the mass fractions satisfy the following relation:

$$\sum_{k \in S} Y_k = 1. \tag{1d}$$

As a result, summing Eq. (1a) for all species and enforcing the mass constraint

$$\sum_{k \in S} \boldsymbol{\mathcal{F}}_k = 0 \tag{1e}$$

gives the equation of total mass conservation

$$\frac{\partial \rho}{\partial t} + \mathrm{div}(\rho \boldsymbol{v}) = 0. \tag{1f}$$

Furthermore, while Eq. (1c) is suitable for computational purposes, it is more convenient, when determining a dispersion relation, to reformulate it as an equivalent equation for the specific enthalpy $\mathfrak{h} = e + p/\rho$,

$$\frac{\partial(\rho \mathfrak{h})}{\partial t} + \mathrm{div}(\rho \mathfrak{h} \boldsymbol{v}) - \frac{\partial p}{\partial t} - \boldsymbol{v} \cdot \mathrm{grad}(p) = -\mathrm{div}(\boldsymbol{\mathcal{Q}}) - \mathbb{T} : \mathrm{grad}(\boldsymbol{v}). \tag{1g}$$

To close the system in Eq. (1), an equation of state is required. The multi-component gas verifies the ideal gas law,

$$p = \rho \frac{R}{M} T = \rho r T, \tag{1h}$$

where $R = 8.3143\ \mathrm{J \cdot mol^{-1} \cdot K^{-1}}$ is the universal gas constant, T is the absolute temperature, $r = R/M$ is the specific gas constant, and M is the mean molar mass of the mixture, defined as

$$\frac{\rho}{M} = \sum_{k \in S} \frac{\rho_k}{M_k}, \tag{1i}$$

where M_k is the molar mass of the kth species. The specific internal energy is expressed as

$$\rho e = \sum_{k \in S} \rho_k e_k, \tag{1j}$$

where e_k is the specific internal energy of the kth species. Each term e_k is a function of temperature only and satisfies the differential,

$$de_k = c_{vk}(T) dT, \tag{1k}$$

where c_{vk} is the constant-volume specific heat of the kth species. The specific enthalpy of the mixture is expressed similarly as

$$\rho \mathfrak{h} = \sum_{k \in S} \rho_k \mathfrak{h}_k, \tag{1l}$$

where $\mathfrak{h}_k = e_k + RT/M_k$ is the specific enthalpy of the kth species. Each term h_k is a function of temperature only and satisfies the differential,

$$dh_k = c_{pk}(T) dT, \tag{1m}$$

where c_{pk} is the constant-pressure specific heat of the kth species. The constant-volume and constant-pressure specific heats of each species c_{vk} and c_{pk}, and of the mixture, c_v and c_p, are defined as follows:

$$c_{vk} = \left[\frac{N_{\mathrm{dof},k} + 2}{2}\right] \frac{R}{M_k}, \quad c_{pk} = c_{vk} + \frac{R}{M_k}, \quad c_v = \sum_{k \in S} Y_k c_{vk}, \quad c_p = \sum_{k \in S} Y_k c_{pk}, \tag{1n}$$

where $N_{\mathrm{dof},k}$ is the number of degrees of freedom of the k th species. Furthermore, the speed of sound of the mixture c is defined as

$$c = \sqrt{\left(\frac{\partial p}{\partial \rho}\right)_{s, Y_1, \ldots, Y_{n_s}}}, \tag{2}$$

where s is the specific entropy, and can be shown to be equal to

$$c = \sqrt{\frac{\gamma p}{\rho}} = \sqrt{\gamma r T}, \tag{3}$$

where $\gamma = c_p/c_v$ is the ratio of specific heats of the mixture.

The transport fluxes $\boldsymbol{\mathcal{F}_k}$, $\mathbb{T}$, and $\boldsymbol{\mathcal{Q}}$ are given by the expressions

$$\boldsymbol{\mathcal{F}}_k = -\sum_{\ell \in S} C_{k\ell} \left[\mathrm{grad}(X_\ell) + (X_\ell - Y_\ell) \frac{\mathrm{grad}(p)}{p} + X_\ell \xi_\ell \frac{\mathrm{grad}(T)}{T}\right], \tag{4a}$$

$$\mathbb{T} = -\left(\mu_b - \frac{2}{3}\mu\right) \mathrm{div}(\boldsymbol{v}) \mathbb{I} - \mu \left[\mathrm{grad}(\boldsymbol{v}) + (\mathrm{grad}(\boldsymbol{v}))^T\right], \tag{4b}$$

$$\boldsymbol{\mathcal{Q}} = -\lambda \mathrm{grad}(T) + \sum_{k \in S} h_k \boldsymbol{\mathcal{F}}_k + \sum_{k \in S} \frac{RT\xi_k}{M_k} \boldsymbol{\mathcal{F}}_k, \tag{4c}$$

where $X_\ell = (M/M_\ell) Y_\ell$ is the mole fraction of the ℓth species, $C_{k\ell}$, $k, \ell \in S$, are the multi-component flux diffusion coefficients (referred to here as species flux coefficients), ξ_ℓ, $\ell \in S$, are the rescaled thermal diffusion ratios, μ_b is the bulk or volume viscosity, μ is the shear viscosity, $\mathbb{I}$ is the identity tensor, and λ is the thermal conductivity. The superscript ^{T} is the transposition operator.

The shear viscosity μ and the thermal conductivity λ are always positive, while the volume viscosity μ_b is zero for monoatomic gases and positive for polyatomic gases. On the contrary, the multi-component flux diffusion coefficients $C_{k\ell}$, $k, \ell \in S$, and the rescaled thermal diffusion ratios ξ_ℓ, $\ell \in S$ can be either positive or negative. Due to the mass constraint [Eq. (1e)], they are required to satisfy the conditions

$$\mathfrak{C} \mathcal{Y} = 0, \quad \langle \mathbf{1}^T, \Xi \mathcal{X} \rangle = \sum_{k \in S} \xi_k X_k = 0, \tag{5}$$

where $\mathfrak{C}$ is the matrix of the multi-component flux diffusion coefficients, $\mathcal{Y} = [Y_1, \ldots, Y_{n_s}]^T$ is the vector of mass fractions, $\mathbf{1} = [1, \ldots, 1]^T$ is a vector of n_s ones, $\Xi = \mathrm{diag}(\xi_1, \ldots, \xi_{n_s})$ is a diagonal matrix whose elements are the rescaled

https://doi.org/10.1121/10.0042249

thermal diffusion ratios, and $\mathcal{X} = [X_1, \ldots, X_{n_s}]^T$ is the vector of mole fractions. In Eq. (5), the operator $\langle \cdot, \cdot \rangle$ indicates the scalar product.

The coefficients $C_{k\ell}$, $k, \ell \in S$, ξ_ℓ, $\ell \in S$, μ_b, μ, and λ, also called transport coefficients, depend on the state variables p, T, and Y_k, $k \in S$, as well as the molecular properties of the gas constituents. These coefficients are obtained by solving linear systems derived from the kinetic theory of gases. For conciseness, these systems are provided in Appendix D.

In a gas mixture, the average velocity of the molecules of a particular species $k \in S$ may differ from the hydrodynamic velocity $\boldsymbol{v}$ of the mixture. This deviation, known as the diffusion velocity $\mathcal{V}_k$, is related to the diffusion flux $\boldsymbol{\mathcal{F}}_k$ by the following expression:

$$\mathcal{V}_k = \frac{\boldsymbol{\mathcal{F}}_k}{\rho Y_k}. \tag{6}$$

Equations (4a) and (6) indicate that the diffusion velocity $\mathcal{V}_k$ includes contributions proportional to the concentration gradients $\mathrm{grad}(X_k)$, the pressure gradient $\mathrm{grad}(p)$, and the temperature gradient $\mathrm{grad}(T)$. The first term corresponds to the well-known Fick's law of ordinary diffusion, also known as Fickian diffusion, which describes the tendency of nonuniform gas mixtures to reduce concentration inhomogeneities. The second term corresponds to barodiffusion, where species migrate in response to a pressure gradient. The third term represents thermal diffusion, also called the Soret effect, which causes molecular species to diffuse in response to temperature gradients.

Additionally, Eq. (4c) highlights the impact of multicomponent effects on heat flux. The first term in Eq. (4c) corresponds to Fourier's law of heat conduction, governing heat transfer due to temperature gradients. The second term accounts for energy transport driven by species diffusion. The final term represents the reciprocal of the Soret effect, describing heat transfer induced by diffusion fluxes.

III. DISPERSION RELATION

A. Assumptions and background atmosphere

This study examines the linear behavior of acoustic and gravity waves propagating through a steady atmosphere with a horizontal background wind. Let $Ox_1x_2x_3$ be a Cartesian coordinate system with the origin at ground level, unit vectors $\mathbf{e}_1, \mathbf{e}_2, \mathbf{e}_3$, and the vertical axis x_3 oriented upward. Any flow variable q is decomposed into a known background value, labeled with the subscript "0", q_0, and a wave-induced perturbation, denoted by the subscript "1," q_1. Thus, $\rho = \rho_0 + \rho_1$, $Y_k = Y_{k,0} + Y_{k,1}$, $k \in S$, $\boldsymbol{v} = \boldsymbol{v}_0 + \boldsymbol{v}_1$, $p = p_0 + p_1$, $T = T_0 + T_1$, etc. The horizontal background velocity $\boldsymbol{v}_0 = v_{0,1}\mathbf{e}_1 + v_{0,2}\mathbf{e}_2$, temperature T_0, and mass fractions $Y_{k,0}$, $k \in S$, are assumed to change gradually in space, with a representative spatial scale $\mathcal{L}$ much larger than the representative wavelength $\mathfrak{L}$. Consequently, all spatial derivatives of $\boldsymbol{v}_0$, T_0, and $Y_{k,0}$, $k \in S$, are on the order of $\mathcal{L}^{-1}$. Neglecting terms of order $\mathcal{O}(\mathcal{L}^{-1})$, the vertical momentum equation yields, in the absence of waves, the hydrostatic balance equation,

$$\frac{\partial p_0(\boldsymbol{x})}{\partial x_3} = -\rho_0(\boldsymbol{x})g(\boldsymbol{x}) = -\frac{p_0(\boldsymbol{x})}{h_0(\boldsymbol{x})}, \tag{7}$$

where

$$h_0(\boldsymbol{x}) = \frac{c_0^2(\boldsymbol{x})}{\gamma_0(\boldsymbol{x})g(\boldsymbol{x})}. \tag{8}$$

The solution to Eq. (7) is

$$p_0(\boldsymbol{x}) = p_0(x_1, x_2, 0)\exp\left(-\int_0^{x_3}\frac{dz}{h_0(\boldsymbol{x})}\right), \tag{9}$$

which gives the background density $\rho_0(\boldsymbol{x})$ as

$$\rho_0(\boldsymbol{x}) = \rho_0(x_1, x_2, 0)\frac{p_0(\boldsymbol{x})h_0(x_1, x_2, 0)}{h_0(\boldsymbol{x})p_0(x_1, x_2, 0)}. \tag{10}$$

Therefore, the vertical profiles of background pressure and density remain locally identical to those in an atmosphere at rest. The function h_0 has the dimensions of length and is referred to as the scale height. No specific assumption is made about its magnitude, which may be much smaller than $\mathcal{L}$. As a result, the spatial derivatives $\partial p_0/\partial x_3$ and $\partial \rho_0/\partial x_3$ are both on the order of h^{-1} and may not be negligible on the wavelength scale $\mathfrak{L}$. In contrast, variations in h_0 and c_0 share the same representative spatial scale $\mathcal{L}$ as the background temperature T_0, meaning that $\partial h_0/\partial x_3$ and $\partial c_0^2/\partial x_3$ are on the order of $\mathcal{L}^{-1}$ and can be neglected at the scale of the wavelength $\mathfrak{L}$.

Finally, the transport coefficients $C_{k\ell}$, $k, \ell \in S$, ξ_ℓ, $\ell \in S$, μ_b, μ, and λ are considered small, implying that the effects of the associated transport fluxes are small on the wavelength scale $\mathfrak{L}$. Their wave-induced perturbations are ignored. Furthermore, since these coefficients depend on temperature T and mass fractions Y_k, $k \in S$, their spatial gradients are on the order of $\mathcal{O}(\mathcal{L}^{-1})$.

B. Linearization

To examine the linear behavior of acoustic and gravity waves under the proposed atmospheric conditions, the wave-perturbation variables, q_1, are assumed to be infinitesimal. Additionally, to derive a system of equations with slowly varying coefficients suitable for asymptotic analysis, these variables are scaled by a factor of $\rho_0^{\pm 1/2}$ as follows (Bergmann, 1946; Gossard and Hooke, 1975; Hines, 1960):

$$\tilde{\rho} = \rho_0^{-1/2}\rho_1, \quad \tilde{p} = \rho_0^{-1/2}p_1, \quad \tilde{\boldsymbol{v}} = \rho_0^{1/2}\boldsymbol{v}_1, \tag{11}$$

$$\tilde{T} = \rho_0^{1/2}T_1, \quad \tilde{Y}_k = \rho_0^{1/2}Y_{k,1}. \tag{12}$$

As a result, under the assumptions of Sec. III A, and neglecting terms on the order of $\mathcal{L}^{-1}$, Eq. (1a) becomes

$$D_{t,0}(\tilde{Y}_k) = -\rho_0^{-1/2}\mathrm{div}\left(\tilde{\boldsymbol{\mathcal{F}}}_{k,1}\right) = \rho_0^{-1/2}\mathrm{div}\left(\sum_{\ell\in S} C_{k\ell,0}\left[\mathrm{grad}\left(\rho_0^{-1/2}\tilde{X}_\ell\right) - \left(\tilde{X}_{\ell,1} - \tilde{Y}_{\ell,1}\right)\frac{\mathbf{e}_3}{\rho_0^{1/2}h_0}\right]\right)$$
$$+ \rho_0^{-1/2}\mathrm{div}\left(\sum_{\ell\in S} C_{k\ell,0}\left[X_{\ell,0}\left(\frac{\mathrm{grad}\left(\rho_0^{1/2}\tilde{p}\right)}{p_0} + \frac{\rho_0^{1/2}\tilde{p}\mathbf{e}_3}{p_0 h_0}\right) + X_{\ell,0}\xi_{\ell,0}\frac{\mathrm{grad}\left(\rho_0^{-1/2}\tilde{T}\right)}{T_0}\right]\right), \tag{13}$$

where $D_{t,0}$ is the operator $D_{t,0}(\,\cdot\,) = \partial(\,\cdot\,)/\partial t + \boldsymbol{v}_0 \cdot \mathrm{grad}(\,\cdot\,)$. Given the assumed small magnitude of the transport fluxes, Eq. (13) indicates that the perturbations of the mass fractions, $\tilde{Y}_k$, $k \in S$, remain small. Consequently, terms proportional to $\tilde{Y}_\ell$ and $\tilde{X}_\ell$ can be neglected in the perturbation of the diffusion flux $\tilde{\boldsymbol{\mathcal{F}}}_{k,1}$. This implies that the perturbation of a mass fraction $\tilde{Y}_k$ depends primarily on the perturbations of pressure $\tilde{p}$ and temperature $\tilde{T}$, and is approximately independent of the perturbations $\tilde{Y}_\ell$, $\ell \neq k$, involving other mass fractions. As a result, barodiffusion and thermodiffusion are the dominant diffusion mechanisms influencing wave propagation, while ordinary diffusion can be neglected. Eq. (1a) can then be rewritten as

$$D_{t,0}(\tilde{Y}_k) = \frac{(\mathfrak{C}_0\mathcal{X}_0)_k}{p_0}\tilde{\Delta}\tilde{p} + \frac{(\mathfrak{C}_0\Xi_0\mathcal{X}_0)_k}{\rho_0 T_0}\tilde{\Delta}\tilde{T}, \quad k \in S, \tag{14a}$$

where the operator Δ is defined by the relation

$$\tilde{\Delta} = \Delta + \frac{1}{h_0}\frac{\partial}{\partial x_3} + \frac{1}{4h_0^2},$$

with Δ the Laplacian operator, and $(\,\cdot\,)_k$ is the kth component of vector $(\,\cdot\,)$.

The linearized equations of mass conservation, momentum, and enthalpy, and the equation of state are rewritten in terms of the scaled variables as follows:

$$D_{t,0}(\tilde{\rho}) + \mathrm{div}(\tilde{\boldsymbol{v}}) - \frac{\tilde{v}_3}{2h_0} = 0, \tag{14b}$$

$$D_{t,0}(\tilde{\boldsymbol{v}}) + \mathrm{grad}(\tilde{p}) - \left(\frac{\tilde{p}}{2h_0} - \tilde{\rho}g\right)\mathbf{e}_3 = -\rho_0^{-1/2}\mathrm{div}(\mathbb{T}_1), \tag{14c}$$

$$D_{t,0}\left(c_{p,0}\tilde{T} - \tilde{p}\right) + g\tilde{v}_3 = -\rho_0^{-1/2}\mathrm{div}\left(\mathcal{Q} - \sum_{k\in S} h_k\boldsymbol{\mathcal{F}}_k\right)_1 - \frac{\langle\mathcal{C}_{p,0}^T, \mathfrak{C}_0\mathcal{X}_0\rangle}{\rho_0 h_0}\left[\frac{\partial\tilde{T}}{\partial x_3} + \frac{\tilde{T}}{2h_0}\right], \tag{14d}$$

$$\tilde{p} = r_0 T_0\tilde{\rho} + r_0\tilde{T} + T_0\langle\mathcal{R}^T, \tilde{\mathcal{Y}}\rangle, \tag{14e}$$

with

$$-\rho_0^{-1/2}\mathrm{div}(\mathbb{T}_1) = \frac{\mu_0}{\rho_0}\tilde{\Delta}\tilde{\boldsymbol{v}} + \frac{\mu_b + \mu_0/3}{\rho_0}\times\left[\mathrm{grad}(\mathrm{div}(\tilde{\boldsymbol{v}})) + \frac{\mathrm{grad}(\tilde{v}_3)}{2h_0} + \frac{\mathrm{div}(\tilde{\boldsymbol{v}})\mathbf{e}_3}{2h_0} + \frac{\tilde{v}_3\mathbf{e}_3}{4h_0^2}\right], \tag{14f}$$

$$-\rho_0^{-1/2}\mathrm{div}\left(\mathcal{Q} - \sum_{k\in S} h_k\boldsymbol{\mathcal{F}}_k\right)_1 = \frac{\lambda_0}{\rho_0}\tilde{\Delta}\tilde{T} + \frac{T_0\langle(\Xi_0\mathcal{R})^T, \mathfrak{C}_0\mathcal{X}_0\rangle}{p_0}\tilde{\Delta}\tilde{p} + \frac{\langle(\Xi_0\mathcal{R})^T, \mathfrak{C}_0\Xi_0\mathcal{X}_0\rangle}{\rho_0}\tilde{\Delta}\tilde{T} - \frac{\langle(\Xi_0\mathcal{R})^T, \mathfrak{C}_0\mathcal{X}_0\rangle}{\rho_0 h_0}\left[\frac{\partial\tilde{T}}{\partial x_3} + \frac{\tilde{T}}{2h_0}\right], \tag{14g}$$

where $\mathcal{C}_p = [c_{p,1}, \ldots, c_{p,n_s}]^T$ is the vector of species-specific heats at constant pressure, $\tilde{\mathcal{Y}} = [\tilde{Y}_1, \ldots, \tilde{Y}_{n_s}]^T$ is the vector of scaled mass-fraction perturbations, and $\mathcal{R} = [R/M_1, \ldots, R/M_{n_s}]^T$ is the vector of specific gas constants.

C. Asymptotic analysis

Given that the characteristic wavelength of interest, $\mathfrak{L}$, is much smaller than the scale $\mathcal{L}$ over which the properties of the background medium vary, insights into the solution of System (14) can be effectively obtained using the method of multiple scales (Anile *et al.*, 1993). Over distances on the order of a wavelength $\mathfrak{L}$, the coefficients from the system in Eq. (14) can be treated as approximately constant, which allows for solutions that locally behave as plane waves. A local plane wave is an expression of the type,

$$\tilde{\boldsymbol{\mathcal{U}}}(\boldsymbol{x}, t) = \hat{\tilde{\boldsymbol{\mathcal{U}}}}(\boldsymbol{x}, t)e^{i\theta(\boldsymbol{x},t)}, \quad \tilde{\boldsymbol{\mathcal{U}}} = \left[\tilde{\rho}, \tilde{\boldsymbol{v}}, \tilde{p}, \tilde{T}, \tilde{Y}_1, \ldots, \tilde{Y}_{n_s}\right]^T, \tag{15}$$

where $\tilde{\boldsymbol{\mathcal{U}}}$ is the vector of the wave variables, $\hat{\tilde{\boldsymbol{\mathcal{U}}}}$ is a complex amplitude vector, and θ is a phase function. If the coefficients in the system in Eq. (14) were constant, as in the case of an isothermal atmosphere, $\hat{\tilde{\boldsymbol{\mathcal{U}}}}$ would be a constant amplitude vector, and the phase function would reduce to $\theta(\boldsymbol{x}, t) = (\boldsymbol{k}\cdot\boldsymbol{x} - \omega t)$, with $\boldsymbol{k}$ a constant wavenumber vector and ω a constant angular frequency. For the local plane wave [Eq. (15)], a local (non-constant) angular frequency

https://doi.org/10.1121/10.0042249

and a local (non-constant) wavenumber vector are defined as follows:

$$\omega(\boldsymbol{x},t) = -\frac{\partial\theta(\boldsymbol{x},t)}{\partial t}, \quad \boldsymbol{k}(\boldsymbol{x},t) = \mathrm{grad}(\theta(\boldsymbol{x},t)). \tag{16}$$

In the method of multiple scales, solutions are sought that depend on the two characteristic scales of the problem: the amplitude $\tilde{\boldsymbol{\mathcal{U}}}$, the wavenumber $\boldsymbol{k}$, and the angular frequency ω are supposed to vary on the scale $\mathcal{L}$ over which the properties of the background medium change; the phase is assumed to change by 2π on the scale of the characteristic wavelength $\mathfrak{L}$. Let $\epsilon = \mathfrak{L}/\mathcal{L}$. Then, $0 < \epsilon \ll 1$ is a dimensionless parameter characteristic of the solution. To proceed further, the slow variables $\boldsymbol{\zeta} = \epsilon\boldsymbol{x}$ and $\tau = \epsilon t$, and the fast variable phase $\theta(\boldsymbol{x},t) = \Theta(\boldsymbol{\zeta},\tau)/\epsilon = \Theta(\epsilon\boldsymbol{x},\epsilon t)/\epsilon$ are defined. Expanding θ as $\epsilon \to 0$, gives

$$\theta(\boldsymbol{x},t) = \frac{1}{\epsilon}\left[\Theta(0) + (\boldsymbol{k}(\boldsymbol{x},t)\cdot\boldsymbol{x} - \omega(\boldsymbol{x},t)t)\epsilon + \mathcal{O}(\epsilon^2)\right],$$

so that θ represents the phase function of a planar wavefront apart from an inessential factor. The local plane wave in Eq. (15) is rewritten as a formal series of the form

$$\tilde{\boldsymbol{\mathcal{U}}}(\boldsymbol{\zeta},\tau,\theta) = e^{i\theta}\sum_{l=0}^{\infty}\epsilon^l\hat{\tilde{\boldsymbol{\mathcal{U}}}}^{(l)}(\boldsymbol{\zeta},\tau). \tag{17}$$

Solutions to the system in Eq. (14) are then sought in the form of Eq. (17), with the spatial and temporal derivatives replaced by the following operators:

$$\begin{aligned}\frac{\partial}{\partial t} &= \frac{\partial\zeta_i}{\partial t}\frac{\partial}{\partial\zeta_i} + \frac{\partial\tau}{\partial t}\frac{\partial}{\partial\tau} + \frac{\partial\theta}{\partial t}\frac{\partial}{\partial\theta} = \epsilon\frac{\partial}{\partial\tau} - \omega\frac{\partial}{\partial\theta},\\ \frac{\partial}{\partial x_j} &= \frac{\partial\zeta_i}{\partial x_j}\frac{\partial}{\partial\zeta_i} + \frac{\partial\tau}{\partial x_j}\frac{\partial}{\partial\tau} + \frac{\partial\theta}{\partial x_j}\frac{\partial}{\partial\theta} = \epsilon\frac{\partial}{\partial\zeta_j} + k_j\frac{\partial}{\partial\theta}.\end{aligned} \tag{18}$$

More specifically, Eq. (17) is required to satisfy the system in Eq. (14) formally as an identity in ϵ. The zeroth-order in ϵ^0 yields a $(5+n_s)\times(5+n_s)$ algebraic system of the form

$$\mathbb{A}_T(\boldsymbol{\zeta},\tau)\hat{\tilde{\boldsymbol{\mathcal{U}}}}^{(0)}(\boldsymbol{\zeta},\tau) = 0, \tag{19}$$

with

$$\mathbb{A}_T = \mathbb{A} + \mu_0\mathbb{A}_\mu + \mu_{b,0}\mathbb{A}_{\mu_b} + \lambda_0\mathbb{A}_\lambda + \mathbb{A}_\mathfrak{b} + \mathbb{A}_\xi, \tag{20}$$

where $\mathbb{A}$ is the matrix that would be obtained in the absence of transport phenomena, and $\mathbb{A}_\mu$, $\mathbb{A}_{\mu_b}$, $\mathbb{A}_\lambda$, $\mathbb{A}_\mathfrak{b}$, and $\mathbb{A}_\xi$ represent the matrices associated with shear viscosity, bulk viscosity, thermal conductivity, barodiffusion, and thermal diffusion, respectively. The system in Eq. (19) has a non-trivial solution for $\hat{\tilde{\boldsymbol{\mathcal{U}}}}^{(0)}$ only if the determinant of $\mathbb{A}_T$ vanishes,

$$\det(\mathbb{A}_T) = 0. \tag{21}$$

As all the transport fluxes are assumed to have a small contribution over distances on the order of a wavelength $\mathfrak{L}$, Eq. (21) is conveniently rewritten as

$$\begin{aligned}\det(\mathbb{A}_T) = \det\big(\mathbb{A} + \varepsilon\big[&(\mu_0\mathbb{A}_\mu + \mu_{b,0}\mathbb{A}_{\mu_b}\\ &+\lambda_0\mathbb{A}_\lambda + \mathbb{A}_\mathfrak{b} + \mathbb{A}_\xi)/\varepsilon\big]\big),\end{aligned} \tag{22}$$

where ε is a small parameter representative of the magnitude of the transport phenomena, and the term within brackets has the same order of magnitude as $\mathbb{A}$. The determinant can then be reformulated via a Taylor expansion based on the derivative of a determinant (Horn and Johnson, 1990),

$$\begin{aligned}\det(\mathbb{A}_T) = \det(\mathbb{A}) + \mathrm{tr}\Big(\mathrm{adj}(\mathbb{A})\big[&\mu_0\mathbb{A}_\mu + \mu_{b,0}\mathbb{A}_{\mu_{b,0}}\\ &+\lambda_0\mathbb{A}_\lambda + \mathbb{A}_\mathfrak{b} + \mathbb{A}_\xi\big]\Big) + \mathcal{O}(\varepsilon^2).\end{aligned} \tag{23}$$

In this form, the determinant of $\mathbb{A}_T$ appears as the sum of the term that would be obtained in the absence of transport phenomena, plus contributions proportional to the transport coefficients. Neglecting terms $\mathcal{O}(\varepsilon^2)$ and equating Eq. (23) to zero finally provides the dispersion relation.

D. Dispersion relation for acoustic and gravity waves in a planetary atmosphere

After some cumbersome algebra, the following dispersion relation is obtained for acoustic and gravity waves:

$$\frac{\omega_d^2}{c_0^2} - \frac{\omega_a^2}{c_0^2} + \frac{\imath\omega_d}{\rho_0 c_0^2}\mathfrak{D} = \left[1 - \frac{\omega_g^2}{\omega_d^2}\right]\boldsymbol{k}_h^2 + k_3^2. \tag{24a}$$

In Eq. (24a), $\omega_d = \omega - \boldsymbol{k}\cdot\boldsymbol{v}_0$ denotes the intrinsic or Doppler-shifted angular frequency, having the meaning of wave angular frequency in a reference frame moving with the local velocity of the background flow, $\omega_a = \gamma_0 g/(2c_0) = c_0/(2h_0)$ is the acoustic cutoff angular frequency, $\omega_g = (\gamma_0 - 1)^{1/2} g/c_0$ is the Brunt-Väisälä angular frequency, and $\boldsymbol{k}_h = k_1\boldsymbol{e}_1 + k_2\boldsymbol{e}_2$ represents the horizontal wavenumber vector. The term $\mathfrak{D}$ incorporates the effects of the transport phenomena and is given by the expression

$$\begin{aligned}\mathfrak{D} = \frac{4\mu_0}{3}B_1 + \mu_{b,0}B_2 + \left[\frac{(\gamma_0-1)\lambda_0}{c_{p,0}} + \mathfrak{t}_0 + \phi_{T,0}\right]B_3\\ + \left[\beta_0 + \phi_{p,0}\right]B_4 + \phi_{h_0,0}B_5,\end{aligned} \tag{24b}$$

where

$$B_1 = \left[1 - \frac{3\omega_g^2\mathbf{k}_h^2 c_0^2}{4\omega_d^4}\right]B_2, \tag{24c}$$

$$B_2 = \boldsymbol{k}_h^2 + \left(k_3 - \frac{\imath}{2h_0}\right)^2, \tag{24d}$$

$$B_3 = \left[1 - \frac{g^2\boldsymbol{k}_h^2}{\omega_d^4}\right]B_2, \tag{24e}$$

$$B_4 = \left[1 + \frac{g}{\omega_d^2}\left(\imath k_3 - \frac{1}{2h_0}\right)\right]B_2, \tag{24f}$$

$$B_5 = \frac{1}{h_0}\left[1 - \frac{g^2 \boldsymbol{k}_h^2}{\omega_d^4}\right]\left[\imath k_3 + \frac{1}{2h_0}\right], \tag{24g}$$

and

$$\beta_0 = \frac{\gamma_0}{r_0}\langle \mathcal{R}^T, \mathfrak{C}_0 \mathcal{X}_0\rangle = \gamma_0 M_0 \sum_{k\in S}\sum_{\ell\in S}\frac{C_{k\ell,0}X_{\ell,0}}{M_k}, \tag{24h}$$

$$\begin{aligned}\phi_{p,0} &= \frac{\gamma_0 - 1}{r_0}\langle (\Xi_0\mathcal{R})^T, \mathfrak{C}_0\mathcal{X}_0\rangle \\ &= (\gamma_0 - 1)M_0 \sum_{k\in S}\sum_{\ell\in S}\frac{\xi_{k,0}C_{k\ell,0}X_{\ell,0}}{M_k},\end{aligned} \tag{24i}$$

$$\begin{aligned}\mathrm{t}_0 &= \frac{\gamma_0 - 1}{r_0}\langle \mathcal{R}^T, \mathfrak{C}_0\Xi_0\mathcal{X}_0\rangle \\ &= (\gamma_0 - 1)M_0 \sum_{k\in S}\sum_{\ell\in S}\frac{C_{k\ell,0}\xi_{\ell,0}X_{\ell,0}}{M_k},\end{aligned} \tag{24j}$$

$$\begin{aligned}\phi_{T,0} &= \frac{(\gamma_0 - 1)^2}{\gamma_0 r_0}\langle (\Xi_0\mathcal{R})^T, \mathfrak{C}_0\Xi_0\mathcal{X}_0\rangle \\ &= \frac{(\gamma_0 - 1)^2 M_0}{\gamma_0}\sum_{k\in S}\sum_{\ell\in S}\frac{\xi_{k,0}C_{k\ell,0}\xi_{\ell,0}X_{\ell,0}}{M_k},\end{aligned} \tag{24k}$$

$$\begin{aligned}\phi_{h_0,0} &= \frac{(\gamma_0 - 1)^2}{\gamma_0 r_0}\langle (\Xi_0\mathcal{R})^T + \mathcal{C}_{p,0}^T, \mathfrak{C}_0\mathcal{X}_0\rangle \\ &= \frac{R}{c_{v,0}c_{p,0}}\sum_{k\in S}\sum_{\ell\in S}C_{k\ell,0}X_{\ell,0}\left[c_{pk,0} + \frac{R\xi_{k,0}}{M_k}\right].\end{aligned} \tag{24l}$$

For vanishing transport coefficients, $\mathfrak{D} = 0$, and Eq. (24) simplifies to the well-known dispersion relation reported by Hines (1960). In the case of a single-species gas, $Y_1 = 1$, $C_{11,0} = \xi_{1,0} = 0$, $\beta_0 = \mathrm{t}_0 = \phi_{p,0} = \phi_{T,0} = \phi_{h_0,0} = 0$, and the dispersion relation derived by Godin (2014) is recovered. The coefficients β_0, t_0, $\phi_{p,0}$, $\phi_{T,0}$, and $\phi_{h_0,0}$ represent specific effects: β_0 accounts for barodiffusion; t_0 arises as a result of thermal diffusion; $\phi_{p,0}$ is associated with heat transfer due to barodiffusion; $\phi_{T,0}$ captures heat transfer induced by thermal diffusion; finally, $\phi_{h_0,0}$ is an additional contribution arising from heat transfer due to species diffusion, which vanishes in the limit of large scale heights, $h_0 \to \infty$.

As reported by Ern and Giovangigli (1994), the matrix with components $C_{k\ell}/Y_k$ is symmetric positive semidefinite. As a result, the coefficients β_0 and $\phi_{T,0}$, which are associated with barodiffusion and heat transfer due to thermal diffusion, are always nonnegative. In contrast, the coefficients t_0 and $\phi_{p,0}$, which stem from thermal diffusion and heat transfer induced by barodiffusion, can be negative, thereby diminishing the overall effect of species diffusion. Furthermore, the symmetry of $C_{k\ell}/Y_k$ implies that the effect of thermal diffusion is identical to that of heat transfer due to barodiffusion, i.e., $\mathrm{t}_0 = \phi_{p,0}$.

In the absence of transport phenomena, propagating waves have real-valued angular frequencies ω_d and wavenumber vectors $\boldsymbol{k}$. However, the transport phenomena, introduced through the term $\mathfrak{D}$ in the dispersion relation in Eq. (24), induce both wave attenuation and dispersion. These effects are captured by the real and imaginary parts of the coefficients B_i, $i = 1, \ldots, 5$, respectively.

The background flow velocity $\boldsymbol{v}_0$ appears in the dispersion relation in Eq. (24) only through the intrinsic frequency ω_d. Its influence on wave propagation, particularly the anisotropy it induces in the attenuation of infrasonic waves, has been discussed by Godin (2014). In the following analysis, a windless atmosphere, where $\boldsymbol{v}_0 = 0$, is considered.

E. Acoustic limit

In the acoustic limit, that is, for $\omega \gg \omega_a$ and $\omega \gg \omega_g$, the effects of gravity and stratification become less pertinent, and the dispersion relation in Eq. (24) reduces to the expression

$$\begin{aligned}\frac{\omega^2}{c_0^2} + \frac{\imath\omega}{\rho_0 c_0^2}\left(\frac{4\mu_0}{3} + \mu_{b,0} + \frac{(\gamma_0 - 1)\lambda_0}{c_{p,0}}\right. \\ \left. + \beta_0 + 2\phi_{p,0} + \phi_{T,0}\right)\boldsymbol{k}^2 = \boldsymbol{k}^2,\end{aligned} \tag{25}$$

which, considering the assumed smallness of the transport coefficients, yields

$$\begin{aligned}\sqrt{\boldsymbol{k}_h^2 + k_3^2} \simeq \frac{\omega}{c_0} + \frac{\imath\omega^2}{2\rho_0 c_0^3}\left(\frac{4\mu_0}{3} + \mu_b + \frac{(\gamma_0 - 1)\lambda_0}{c_{p,0}}\right. \\ \left. + \beta_0 + 2\phi_{p,0} + \phi_{T,0}\right).\end{aligned} \tag{26}$$

The imaginary part of the right-hand side of Eq. (26) represents a spatial attenuation rate, labeled as α, also referred to as the absorption coefficient. It can be written as

$$\alpha = \underbrace{\alpha_{\mu_0} + \alpha_{\mu_{b,0}} + \alpha_{\lambda_0}}_{\alpha_{\text{classical}}} + \alpha_{\text{diffusion}}, \tag{27a}$$

with

$$\alpha_{\mu_0} = \frac{\omega^2}{2\rho_0 c_0^3}\frac{4\mu_0}{3}, \tag{27b}$$

$$\alpha_{\mu_{b,0}} = \frac{\omega^2}{2\rho_0 c_0^3}\mu_b, \tag{27c}$$

$$\alpha_{\lambda_0} = \frac{\omega^2}{2\rho_0 c_0^3}\frac{(\gamma_0 - 1)\lambda_0}{c_{p,0}}, \tag{27d}$$

$$\alpha_{\text{diffusion}} = \frac{\omega^2}{2\rho_0 c_0^3}\left[\beta_0 + 2\phi_{p,0} + \phi_{T,0}\right]. \tag{27e}$$

The sum of the first three terms, originating from viscous stresses and thermal conduction (Kirchhoff, 1868), represents the classical Stokes–Kirchhoff absorption coefficient

https://doi.org/10.1121/10.0042249

$\alpha_{\text{classical}}$. On the other hand, the term $\alpha_{\text{diffusion}}$ is an absorption coefficient associated with species diffusion in a multicomponent gas. For a binary mixture, Eq. (27e) simplifies to the expression reported by Kohler (1941). Specifically, the coefficients β_0, t_0, $\phi_{p,0}$, and $\phi_{T,0}$ take the following forms:

$$\beta_0^{\text{bin}} = \gamma_0 \rho_0 \mathcal{D}_{12,0}^{\text{bin}} Y_{1,0}(1 - Y_{1,0}) \frac{[M_2 - M_1]^2}{M_1 M_2}, \tag{28a}$$

$$\phi_{p,0}^{\text{bin}} = \mathrm{t}_0^{\text{bin}} = (\gamma_0 - 1)\rho_0 \mathcal{D}_{12,0}^{\text{bin}} \frac{\xi_{1,0} Y_{1,0}[M_2 - M_1]}{M_1}, \tag{28b}$$

$$\phi_{T,0}^{\text{bin}} = -\frac{(\gamma_0 - 1)^2}{\gamma_0} \rho_0 \mathcal{D}_{12,0}^{\text{bin}} \xi_{1,0} \xi_{2,0}, \tag{28c}$$

where the superscript $^{\text{bin}}$ indicates the quantity applies to a binary mixture, the subscripts "1" and "2" represent the species pair (1,2), and $\mathcal{D}_{12,0}^{\text{bin}}$ represents the binary diffusion coefficient of the species pair "1" and "2" (see Appendix D). As will be demonstrated, the barodiffusion term β_0 represents the dominant contribution to attenuation due to species diffusion in all atmospheres considered. Eq. (28a) indicates that, for fixed mass fractions, β_0^{bin} is larger when the species have significantly different molar masses, whereas it remains small when their molar masses are similar. This trend holds not only for binary mixtures, but for general mixtures of n_s gases.

IV. ATTENUATION OF ACOUSTIC WAVES IN PLANETARY ATMOSPHERES

This section focuses on analyzing acoustic wave attenuation in planetary atmospheres. Specifically, the attenuation coefficient α [see Eq. (27)] is computed as a function of frequency $f = \omega/(2\pi)$ and altitude x_3 for the atmospheres of Earth, Venus, and Mars. Three outer solar system bodies—Titan, Uranus, and Neptune—were also considered, and their results are shown in detail in Appendix B. The frequencies considered here focus on $f \leq 10$ Hz, specifically lower-frequency infrasound, as these waves can propagate to high altitudes in planetary atmospheres.

The required atmospheric input parameters include the vertical profiles of mole fractions, $X_{k,0}(x_3)$, for each species $k \in S$, the temperature vertical profile, $T_0(x_3)$, and the ground pressure $p_0(x_3 = 0)$. The atmospheric molar mass, $M_0(x_3)$, is determined via the expression $M_0(x_3) = \sum_{k \in S} X_{k,0}(x_3) M_k$. From this, the mass fractions, $Y_k(x_3)$, are computed via the formula $Y_{k,0}(x_3) = M_k X_{k,0}(x_3)/M_0(x_3)$. The specific gas constant follows as $r_0(x_3) = R/M_0(x_3)$. The specific heats are evaluated using Eq. (1n), allowing for the computation of the specific heat ratio $\gamma_0(x_3) = c_p(x_3)/c_v(x_3)$. The speed of sound profile, $c_0(x_3)$, is then given by $c_0(x_3) = \sqrt{\gamma_0(x_3) r_0(x_3) T_0(x_3)}$.

The gravitational acceleration at altitude x_3, $g(x_3)$, is provided by Newton's law

$$g(x_3) = \frac{G \mathfrak{M}_{\text{planet}}}{\left(\mathfrak{R}_{\text{planet}} + x_3\right)^2}, \tag{29}$$

where $G = 6.67430 \times 10^{-11}$ N · m^2 · kg^{-2} is the gravitational constant, and $\mathfrak{M}_{\text{planet}}$ and $\mathfrak{R}_{\text{planet}}$ represent the planet's mass and reference radius, respectively.

The vertical pressure profile, $p_0(x_3)$, is obtained numerically by integrating Eq. (9) from the surface, $x_3 = 0$, to the maximum altitude of interest. The density profile, $\rho_0(x_3)$, is then derived from the equation of state Eq. (1h).

Finally, given the mole fraction vertical profiles $X_{k,0}(x_3)$ and the temperature profile $T_0(x_3)$, the transport coefficients – $\mu_0(x_3)$, $\mu_{b,0}(x_3)$, $\lambda_0(x_3)$, $C_{k\ell,0}(x_3)$, $k, \ell \in S$, and $\xi_{k,0}$, $k \in S$ – are computed by solving the transport linear systems described in Appendix D.

The atmospheric input profiles–$X_{k,0}(x_3)$ or $Y_{k,0}(x_3)$ for each species $k \in S$, as well as $T_0(x_3)$ and the surface pressure $p_0(x_3 = 0)$–are taken from the NRLMSISE-00 model (Picone *et al.*, 2002) for Earth, and from the NASA-GRAM suite (Justh and Hoffman, 2020; Justus *et al.*, 1996) for Venus, Mars, Titan, Uranus, and Neptune. Table I summarizes the atmospheric parameters for Earth, Venus, and Mars used in this study.

While the following figures display full atmospheric profiles (from the surface up to 350 km), our analysis focuses on the upper atmosphere–particularly altitudes above 120 km–where classical attenuation mechanisms and species diffusion become more pronounced, and vibrational relaxation effects generally decrease. Vibrational relaxation is well known to impact the lower atmosphere (Gillier *et al.*, 2024; Sutherland and Bass, 2004; Trahan and Petculescu, 2020), and Fig. 14, along with the corresponding discussion, addresses this additional relaxation. For this analysis, however, we focus on species diffusion relative to classical dissipative mechanisms, which dominate at higher altitudes.

A. Results

1. Earth

Figure 1 shows representative vertical profiles of Earth's atmosphere from the surface to 350 km altitude at 90° N, 0° W in December. This profile was selected to

TABLE I. Planetary parameters used for Earth, Venus, and Mars atmospheric models.

Planet	Mass $\mathfrak{M}_{\text{planet}}$[kg]	Radius $\mathfrak{R}_{\text{planet}}$[km]	Atmospheric model	Latitude	Longitude	Ground pressure $p_0(x_3 = 0)$[Pa]
Earth	5.972×10^{24}	6378	MSIS-00	90°N	0°W	9.812×10^4
Venus V1	4.867×10^{24}	6051	GRAM	22°N	48°W	92.06×10^5
Venus V2	4.867×10^{24}	6051	GRAM	22°N	48°W	92.09×10^5
Mars	6.39×10^{23}	3389.5	GRAM	45°N	48°W	619.4

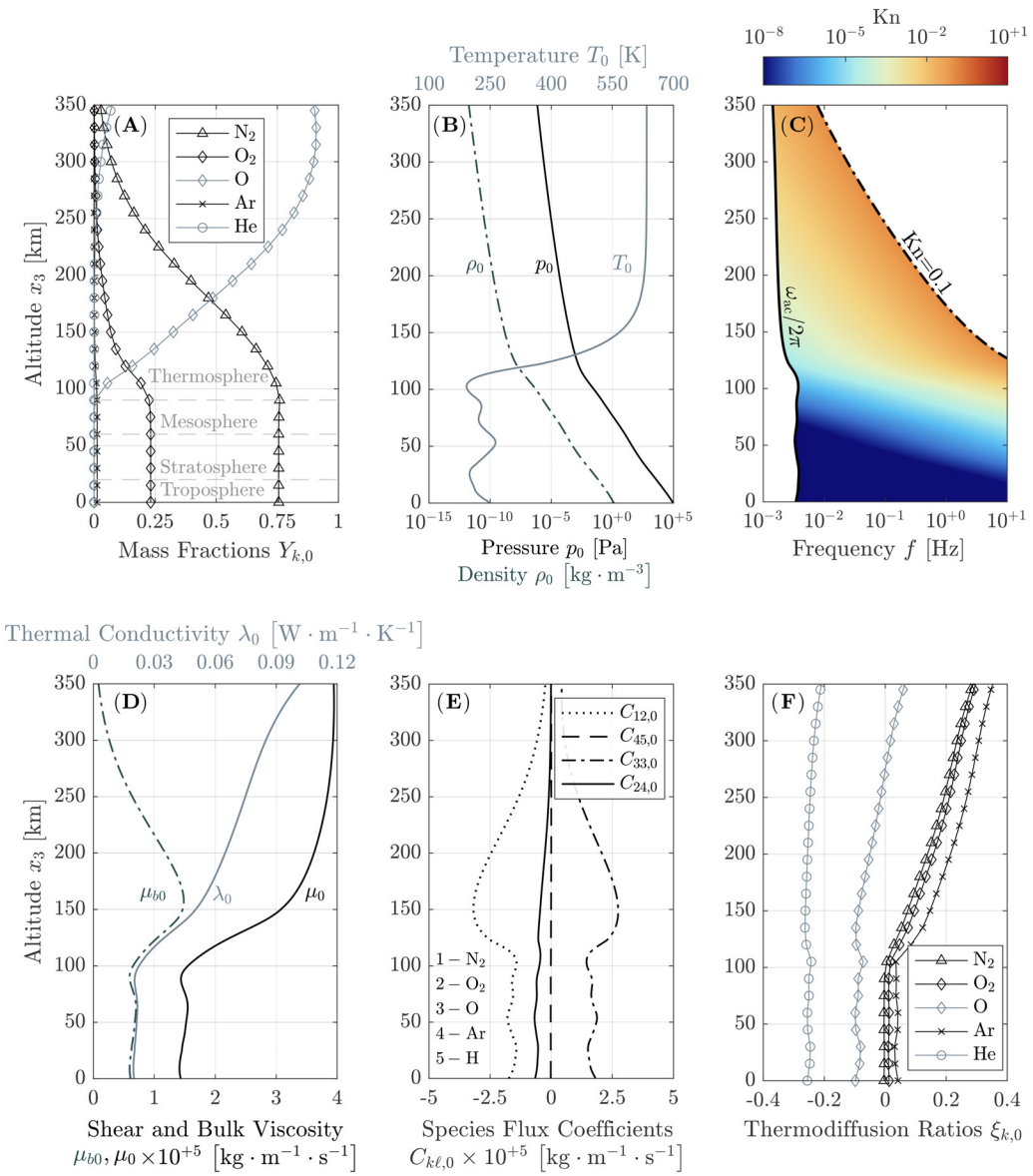

FIG. 1. Representative vertical profiles for Earth's atmosphere.

reflect the full range of possible atmospheric compositions in the upper thermosphere, including the presence of helium (He) above 300 km. While the lower thermosphere typically consists primarily of N_2, O_2, and atomic oxygen (O), the inclusion of He provides a case where lighter species are appreciable, allowing us to examine the upper limit of species diffusion effects on acoustic attenuation.

Figure 1(A) displays the mass fractions $Y_{k,0}$ of major atmospheric constituents. Below ∼100 km, the atmosphere behaves as a binary mixture of N_2 and O_2. Between 100 and 250 km, increasing O transitions the composition into a ternary mixture. Above 300 km, He becomes significant, further modifying the composition.

Figure 1(B) shows the corresponding vertical profiles of temperature T_0, pressure p_0, and density ρ_0. The temperature is around 210 K below ∼100 km altitude, then increases sharply in the thermosphere, reaching values near 560 K above 150 km altitude. Due to gravitational stratification, both p_0 and ρ_0 decrease exponentially, spanning more than ten orders of magnitude over the altitude range 0–350 km.

Figure 1(C) presents the vertical evolution of the frequency-based Knudsen number, $\mathrm{Kn} = \ell_{\mathrm{fp}} f / c_0$, which quantifies the ratio between the molecular mean free path ℓ_{fp} (microscopic scale) and the acoustic wavelength c_0/f (macroscopic scale). The spatial attenuation rate given by Eq. (27) is derived under the continuum assumption, which requires macroscopic length scales to be much larger than microscopic ones. We adopt $\mathrm{Kn} \simeq 0.1$ as a practical upper bound for validity. The panel also reports the acoustic cutoff frequency, below which acoustic propagation is not supported. As altitude increases, the growing mean free path reduces the range of frequencies for which the continuum model remains valid. At approximately $x_3 = 300$ km, valid results are limited to the range $\sim 10^{-3}$ Hz to 0.1 Hz.

Figure 1(D) presents the vertical profiles of dynamic viscosity, bulk viscosity, and thermal conductivity. The

https://doi.org/10.1121/10.0042249

dynamic viscosity and thermal conductivity generally follow the temperature profile. In contrast, the bulk viscosity—nonzero only in polyatomic gases—aligns with temperature only up to ∼150 km, after which it decreases rapidly due to the increasing abundance of O.

Figure 1(E) presents selected elements $C_{k\ell,0}$ of the multi-component diffusion matrix, while Fig. 1(F) shows the rescaled thermodiffusion ratios $\xi_{k,0}$. The elements $C_{12,0}$ and $C_{33,0}$ represent interactions between N_2 and O_2, and self-diffusion of O, respectively. These coefficients are symmetric and reflect the underlying mass conservation constraints of the system. The thermodiffusion ratios exhibit similar trends and structural features.

Figure 2(A) illustrates the spatial attenuation rate α (in dB · km^{-1}) as a function of frequency f and altitude x_3. Attenuation increases proportionally to the square of the frequency, f^2, and inversely to the atmospheric density, $1/\rho_0$. Since ρ_0 decays exponentially with altitude, α likewise increases exponentially. For instance, at $f = 10^{-2}$ Hz, α is approximately 4.05×10^{-5} dB · km^{-1} at 100 km and rises to roughly 0.587 dB · km^{-1} at 300 km.

Figure 2(B) quantifies the percentage contributions of individual transport mechanisms to the attenuation coefficient α. Viscous shear stresses dominate across the entire altitude range, accounting for 50%–60% of total attenuation. Thermal conduction contributes 20%–40%, followed by bulk viscosity (up to ∼20%), and species diffusion (up to ∼16%).

Figure 2(C) further resolves the role of individual species diffusion processes. Barodiffusion (β_0) is the primary contributor. In contrast, thermodiffusion (t_0) and heat transfer due to barodiffusion ($\phi_{p,0}$) are negative, partially offsetting the overall impact of species diffusion. Finally, heat transfer due to thermodiffusion ($\phi_{T,0}$) is negligible throughout the considered altitude range.

2. Venus

Figure 3 presents vertical profiles of two representative Venusian atmospheric states, labeled V1 and V2, spanning altitudes from the surface to 350 km at 22°, N latitude, 48°, W. V1 [Figs. 3(A)–3(C)] corresponds to conditions during a period of elevated solar insolation, such as near Venus's superior conjunction, when enhanced solar input drives increased upper-atmospheric photochemistry. V2 [Figs. 3(D)–3(F)] represents a state with reduced solar activity, characterized by lower thermospheric temperatures and diminished oxygen abundance.

Below 100 km, both profiles exhibit similar properties: the atmosphere is dense [$\rho_0(x_3 = 0) \approx 65$ kg · m^{-3}], primarily composed of 95%–98% CO_2 and 2%–3% N_2, with a surface temperature of approximately 735 K. However, above 150 km, significant differences emerge. V1 is dominated by O (∼95%), with minor fractions of N_2, CO, and He. In contrast, V2 reaches a maximum oxygen concentration of 86% near 180 km, but O is gradually replaced by He and H at higher altitudes. Furthermore, V2 remains denser and cooler than V1 above 100 km.

The transport coefficients for both V1 and V2 profiles are shown in Fig. 7 in Appendix A. Despite substantial differences in composition, particularly in the upper atmosphere, the viscosity and bulk viscosity profiles are nearly identical between the two cases, and thermal conductivity differs by up to 15%, with V2 exhibiting higher values at greater altitudes. In contrast, the species flux coefficients and thermodiffusion ratios show stronger sensitivity to composition. For instance, the thermodiffusion ratio of helium remains negative and asymptotically approaches zero in V1, while in V2 it becomes positive with increasing altitude. A similar divergence appears in the species flux coefficient $C_{46,0}$ (He-O interaction), which increases with altitude in V1

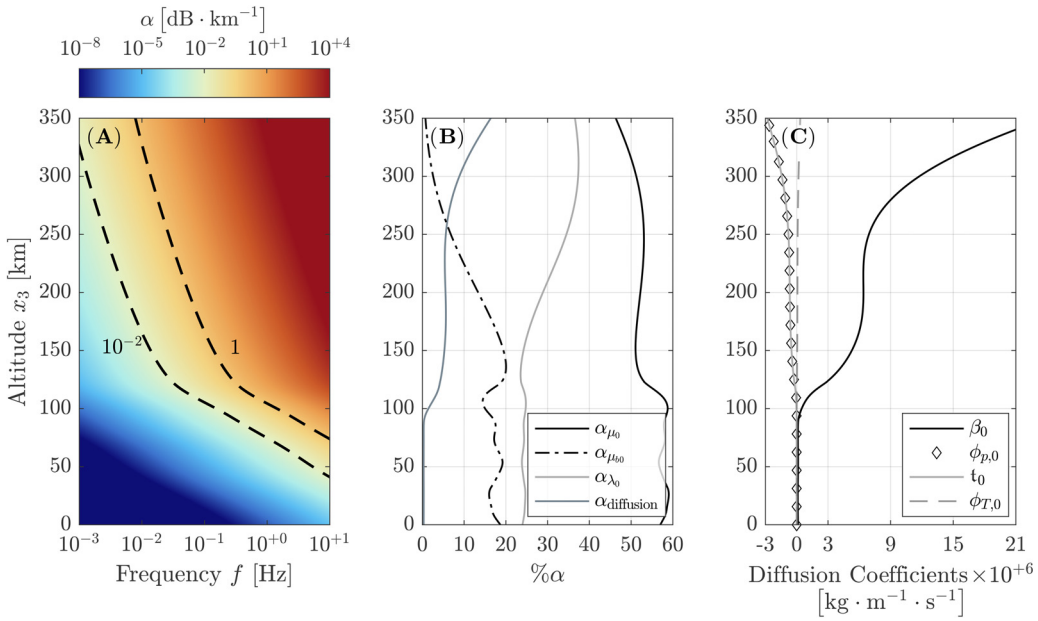

FIG. 2. Attenuation of acoustic waves in Earth's atmosphere.

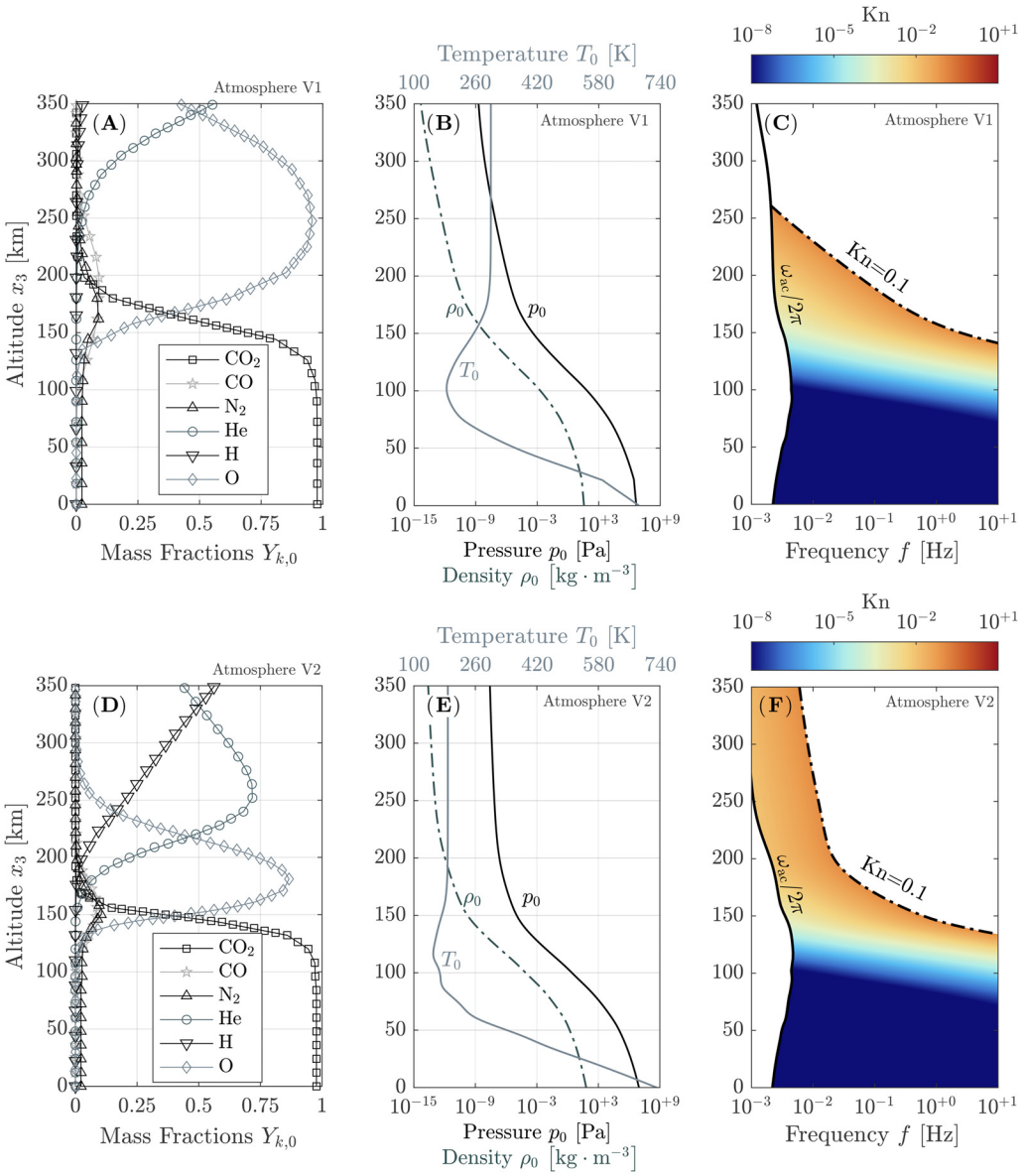

FIG. 3. Representative vertical profiles for two Venusian atmospheric models.

but decreases around 250 km in V2 due to differing helium and oxygen abundances. These compositional sensitivities directly affect the attenuation due to species diffusion, as the relevant transport coefficients appear proportionally in the formulation. A more detailed analysis of these differences is provided in Appendix A.

These differences have a direct impact on acoustic wave propagation in the upper atmosphere, as shown in Figs. 3(C) and 3(F). In V2, the acoustic cutoff frequency decreases to $f \sim 10^{-4}$ Hz above 250 km, permitting the transmission of lower-frequency infrasonic waves. In contrast, in V1, the cutoff frequency remains above 10^{-3} Hz up to 300 km, thereby limiting the range of propagating frequencies even moreso than V2. Additionally, V2 supports a broader altitude range where the frequency-based Knudsen number remains below the continuum threshold (Kn < 0.1), broadening the applicable range of the attenuation model relative to V1.

The influence of species diffusion on total acoustic attenuation is illustrated in Figs. 4(A)–4(C) for V1 and Figs. 4(D)–4(F) for V2. Below 100 km, attenuation remains low for frequencies up to 10 Hz, with $\alpha \approx 1.7 \times 10^{-9}$ dB · km^{-1} in V1 and 1.5×10^{-9} dB · km^{-1} in V2 at $x_3 = 50$ km and $f = 0.1$ Hz. In this region, species diffusion contributes negligibly (<0.4% of α). At higher altitudes, around $x_3 = 150$ km, diffusion-induced attenuation reaches a local maximum, accounting for approximately 13% of total attenuation in V1 and 15% in V2.

Above 150 km, attenuation due to species diffusion increases markedly in V2, reaching 27.75% of total attenuation at $x_3 = 200$ km. In contrast, the contribution from species diffusion in V1 at the same altitude decreases to 4.16%. At $x_3 = 200$ km and $f = 0.01$ Hz, the total attenuation α is 1.27 dB · km^{-1} in V1 and 5.84 dB · km^{-1} in V2. This discrepancy is primarily driven by the enhanced contribution of

https://doi.org/10.1121/10.0042249

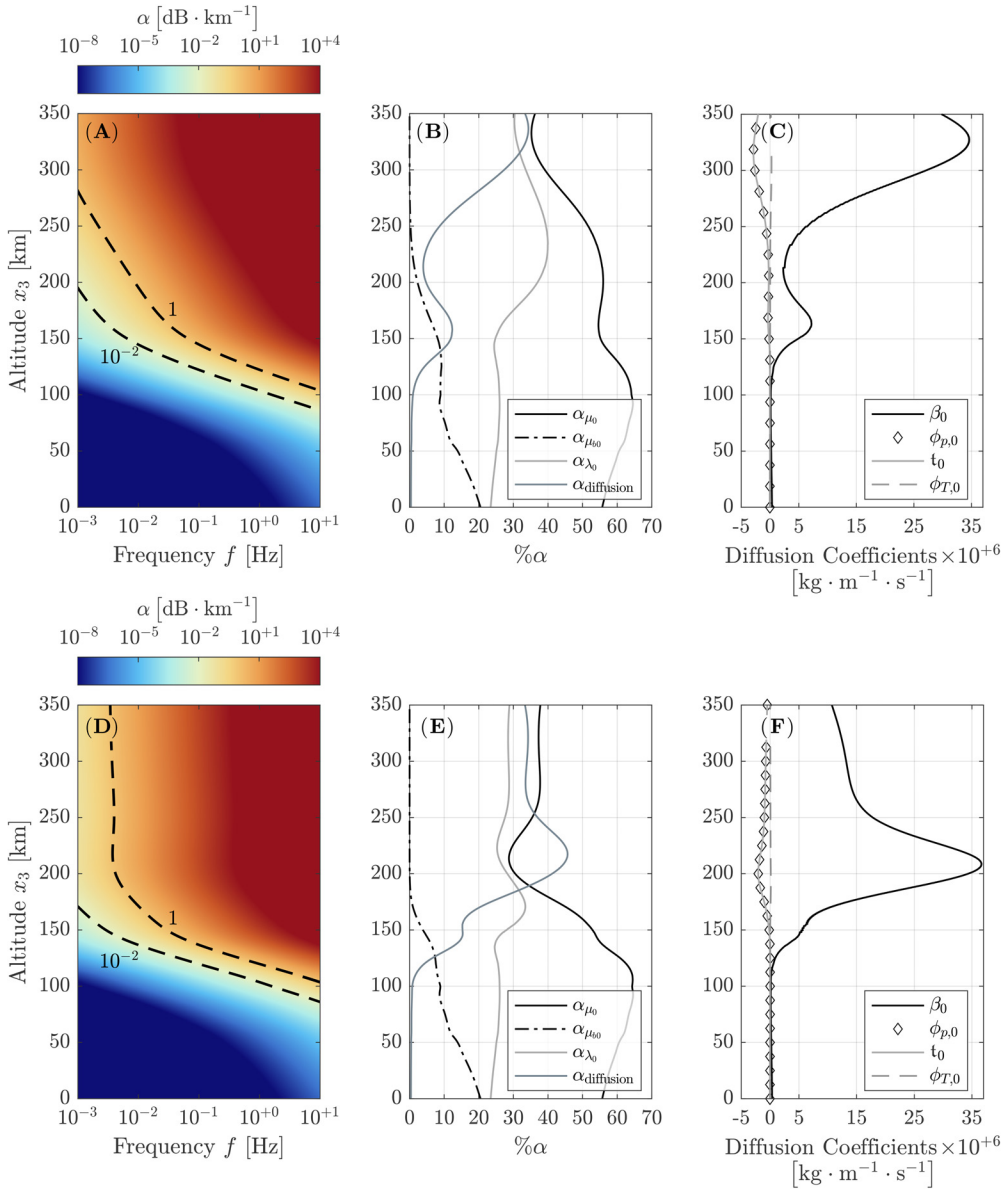

FIG. 4. Attenuation of acoustic waves in two Venusian atmospheres.

species diffusion in V2; when diffusion is excluded from the calculation, attenuation levels in the two atmospheres become nearly identical.

Attenuation arising from shear viscosity and thermal conductivity remains similar in V1 [Fig. 4(A)] and V2 [Fig. 4(D)], as the temperature and density profiles of the two atmospheres are broadly comparable. Bulk viscosity closely follows the CO_2 concentration in both cases, since CO_2 is the only polyatomic species present in significant amounts. In V1, the contributions of thermal conduction (α_{λ_0}) and shear stresses (α_{μ_0}) to the total attenuation range from 20%–40% and 38%–62%, respectively. In V2, α_{λ_0} remains within a similar range, while α_{μ_0} exhibits greater variability (28%–62%).

Figures 4(C) and 4(F) show the diffusion coefficients used to compute species diffusion for V1 and V2, respectively. In both cases, the dominant contribution arises from barodiffusion (β_0), with smaller corrections from the thermodiffusion coefficients t_0 and $\phi_{T,0}$. The barodiffusion coefficient reaches similar peak values in both profiles, $\max(\beta_0) \approx 37 \times 10^{-6}$ kg · m · s^{-1}. However, this maximum occurs at 325 km in V1—outside the region where the Knudsen number remains valid—while in V2, a comparable value is reached near 200 km.

3. Mars

Figure 5 presents representative vertical profiles of the Martian atmosphere from the surface up to 350 km altitude, corresponding to conditions at 45° N, 48° W during the month of August.

As on Venus, the lower Martian atmosphere is primarily composed of CO_2, with trace amounts of molecular nitrogen (N_2) and argon (Ar)—see Fig. 5(A). Unlike Venus, however, Mars' atmosphere is significantly less dense, especially in

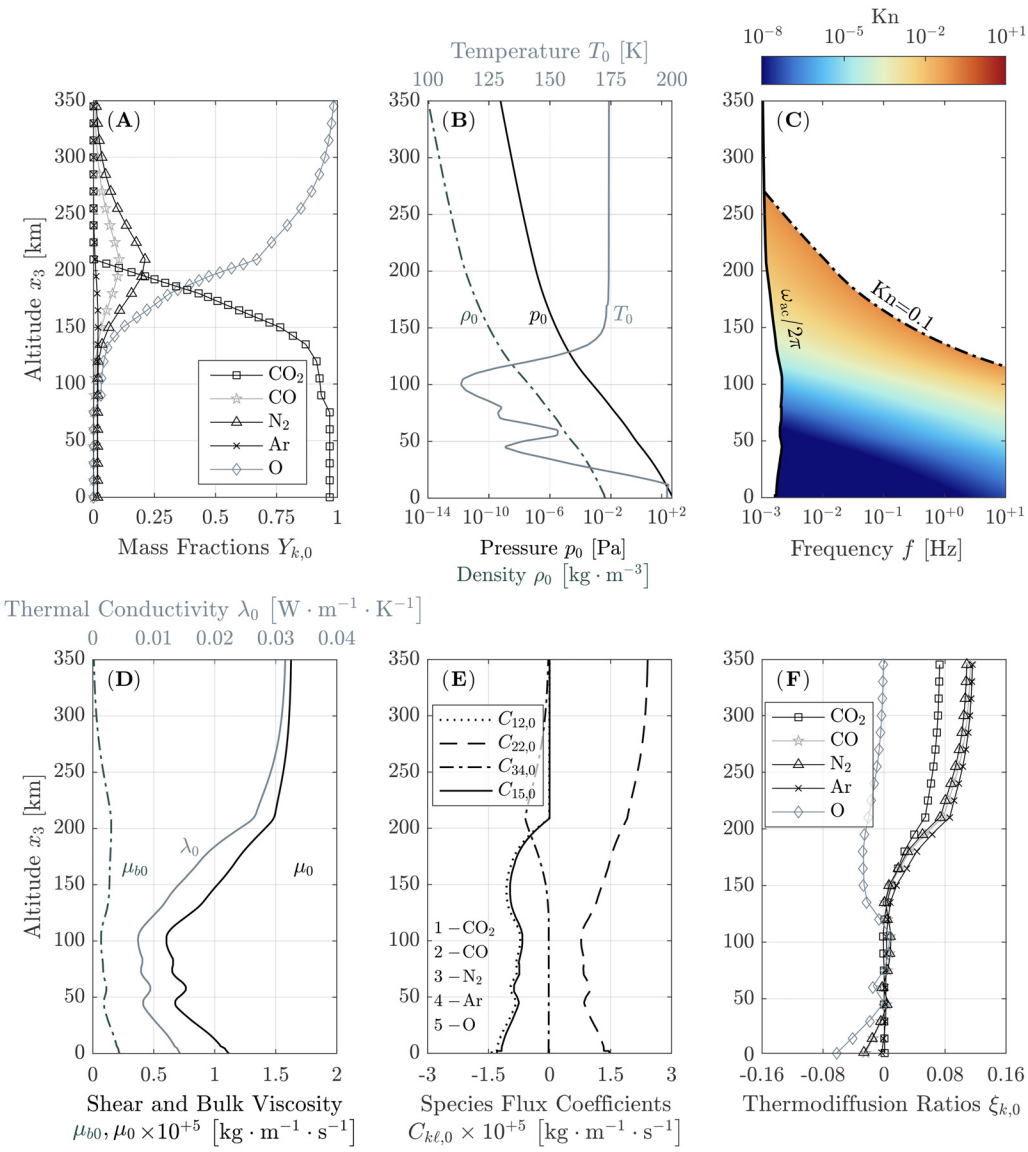

FIG. 5. Representative vertical profiles for a Martian atmosphere.

the lower atmosphere. As shown in Fig. 5(B), the surface density is $\rho_0(x_3 = 0\,\mathrm{km}) = 0.161\,\mathrm{kg \cdot m^{-3}}$ and the surface pressure is $p_0(x_3 = 0) = 585\,\mathrm{Pa}$. CO_2 remains the dominant constituent up to $x_3 = 160$ km, where a compositional transition occurs. Above this altitude, the atmosphere is increasingly dominated by O, with carbon monoxide (CO), N_2, and residual CO_2 as minor species, along with traces of Ar. The upper atmosphere is characterized by low temperatures [$T_0(x_3 > 150\,\mathrm{km}) \approx 140\,\mathrm{K}$] and extremely low density and pressure [$\rho_0(x_3 > 150\,\mathrm{km}) < 10^{-10}\,\mathrm{kg \cdot m^{-3}}$, $p_0(x_3 > 150\,\mathrm{km}) < 10^{-6}\,\mathrm{Pa}$].

Figure 5(C) shows the frequency-dependent Knudsen number (Kn) as a function of altitude and frequency. As on other planets, the range of frequencies over which the continuum approximation remains valid narrows with increasing altitude. At approximately $x_3 = 200$ km, the continuum regime is restricted to a frequency band of roughly 1.1×10^{-3} Hz to 15×10^{-3} Hz.

Mars' low temperatures and weak vertical temperature gradient are reflected in the relatively constant profiles of the transport coefficients, shown in Figs. 5(D)–5(F). Below $x_3 = 150$ km, the temperature varies modestly, but the composition remains dominated by CO_2, with trace amounts of N_2, and the atmosphere behaves effectively as a single-component gas. Above 150 km, this pattern reverses: the temperature becomes more uniform while the composition transitions to a quaternary mixture as CO_2 concentrations decline. This compositional shift introduces variability in the transport coefficients. Viscosity and thermal conductivity increase with altitude above 150 km, while below this threshold, they follow the temperature profile. The multicomponent flux coefficients also begin to vary above 150 km, reflecting increased species separation. Likewise, thermodiffusion ratios, which are negligible below 150 km, begin to diverge at higher altitudes. Despite having transport coefficients comparable to those of Earth and Venus, Mars

https://doi.org/10.1121/10.0042249

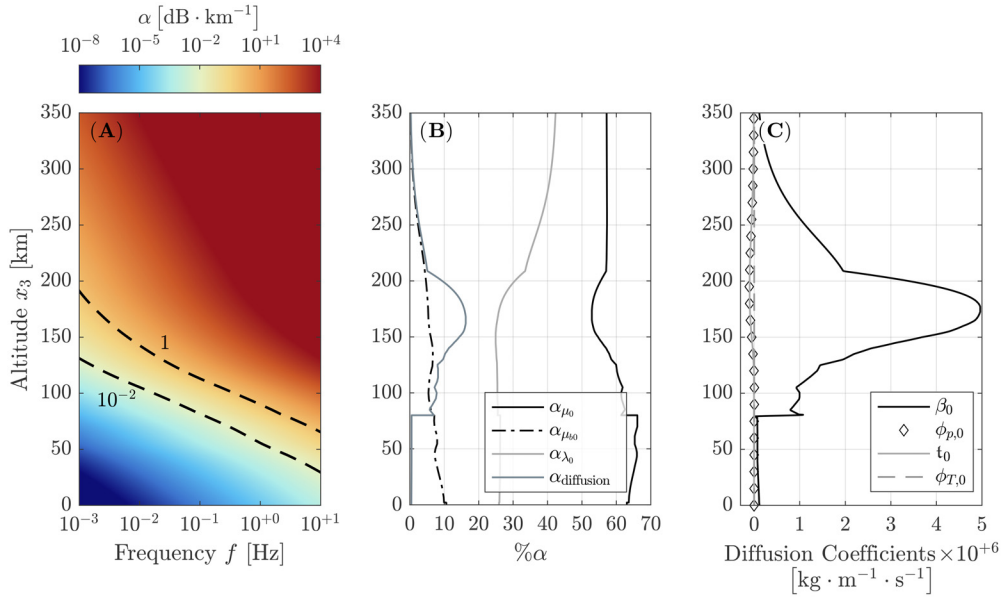

FIG. 6. Attenuation of acoustic waves in a Martian atmosphere.

exhibits the highest overall acoustic attenuation due to its compositional and thermal structure.

Figure 6 illustrates the attenuation properties of Mars. Figure 6(A) shows the total acoustic attenuation coefficient α as a function of altitude and frequency. For the frequency and altitude ranges considered, attenuation on Mars exceeds that on Earth. For example, at $f = 0.01$ Hz and $x_3 = 200$ km, attenuation on Mars reaches 3.04 dB $\cdot$ km^{-1}, which is approximately 80 times greater than that on Earth at the same altitude and frequency.

As on Earth and Venus, viscous shear stresses are the dominant mechanism of acoustic attenuation on Mars. Below 80 km, they account for 74–76% of the total attenuation, gradually decreasing to 58% at $x_3 = 200$ km. Thermal conduction contributes approximately 16% below 160 km, increasing to 30% at higher altitudes. Species diffusion is negligible below 80 km but becomes increasingly significant above this altitude, reaching a maximum contribution of 17% at $x_3 = 155$ km. Finally, bulk viscosity contributes approximately 10% of the total attenuation near the surface and decreases steadily with altitude, falling to 3% at $x_3 = 200$ km.

While species diffusion significantly affects acoustic attenuation on Earth, Venus, and Mars, we find it to be negligible on Uranus, Neptune, and Titan. These atmospheric and attenuation profiles are included in Appendix B (see Figs. 8–13) for completeness.

B. Discussion

Our results demonstrate that species diffusion can substantially increase acoustic attenuation in the upper atmospheres of Earth, Venus, and Mars, especially at altitudes above 150 km. In contrast, its influence is considerably weaker in the upper atmospheres of Titan, Uranus, and Neptune. Among the different species diffusion mechanisms considered, barodiffusion—driven by pressure gradients—emerges as the primary contributor to this enhanced attenuation. Thermodiffusion, driven by temperature gradients, consistently opposes the effect of barodiffusion and acts as a corrective mechanism, typically reducing the net attenuation. Despite its opposing sign, the behavior of thermodiffusion closely mirrors that of barodiffusion: it peaks in the same regions and follows a similar spatial structure. However, its magnitude remains comparatively small, contributing less than 20% of the barodiffusion-driven attenuation in most cases.

By comparison, ordinary diffusion, which arises from concentration gradients, plays a negligible role in acoustic attenuation and does not appear in Eq. (27). Although ordinary diffusion contributes to species transport in the upper atmosphere, its influence on sound attenuation is minimal. This behavior stems from the nature of acoustic waves, which induce only small perturbations in species mass fractions (Y_k'), yielding vanishingly small concentration gradients ($\nabla Y_k'$) and, consequently, a negligible ordinary diffusion flux.

The impact of barodiffusion is most pronounced in gas mixtures with large molar mass contrasts. This behavior can be qualitatively explained by examining the limiting form of the generalized barodiffusion coefficient for a binary mixture, β_0^{bin} [Eq. (28a)]. In this simplified case, β_0^{bin} scales with both the binary diffusion coefficient and a mass contrast term, $(M_2 - M_1)^2/M_1M_2$, which becomes large when heavy and light gases are present in comparable proportions. The full multi-component formulation given by Eq. (24h) captures simultaneous interactions among all species; it can be understood conceptually as a weighted combination of binary interactions, where the effective transport coefficients adjust according to the mixture's composition and complexity.

Earth's atmosphere serves as a clear example. Below 100 km, it is primarily composed of N_2 and O_2, which have comparable molar masses. As a result, species diffusion-induced attenuation is negligible, consistent with earlier findings (Sutherland and Bass, 2004). However, above ~150 km, O becomes increasingly abundant, leading to a noticeable increase in the attenuation coefficient. Using Eq. (28a), attenuation due to species diffusion can be compared between these two regions: the lower atmosphere—approximated as a binary mixture of N_2 and O_2—and the upper atmosphere, where a binary mixture of N_2 and O serves as a representative model. Although the diffusion coefficient for N_2-O is only moderately larger than that of N_2–O_2 ($\mathcal{D}^{\text{bin}}_{N_2-O} \approx 1.5\,\mathcal{D}^{\text{bin}}_{N_2-O_2}$), the corresponding mass contrast term is nearly 20 times greater. As a result, species diffusion accounts for approximately 5%–6% of total acoustic attenuation between 150 and 250 km, increasing to ~16% above 250 km as helium becomes more abundant.

This pattern highlights a broader principle: attenuation due to species diffusion is greatest when both heavy and light molecular species coexist in significant relative concentrations. This effect accounts for the pronounced difference between the two Venusian atmospheric profiles shown in Fig. 4. Although the temperature, pressure, and density profiles differ by less than 20% between the two cases, species diffusion contributes 45% of total acoustic attenuation in Atmosphere V2—more than double the 17% contribution observed in Atmosphere V1. The enhanced attenuation in V2 arises from higher abundances of light species such as O, H, and He in its upper layers.

Mars exhibits a similar pattern of altitude-dependent species diffusion effects. Below 80 km, the atmosphere is dominated by carbon dioxide (CO_2) with only trace amounts of N_2, resulting in negligible attenuation from species diffusion. At higher altitudes, however, increasing concentrations of CO, O, and N_2 enhance barodiffusion, which peaks at 17% of the total attenuation α at $x_3 = 155$ km. At this altitude, the atmospheric composition forms a quaternary mixture of CO_2, O, CO, and N_2. The largest contribution to the barodiffusion coefficient arises from the CO_2–O pair. However, neglecting interactions among the full set of species leads to significant underestimation. For example, a simplified binary model that includes only CO_2 and O underpredicts diffusion-related attenuation by nearly 50%.

We applied the same modeling framework to Titan, Uranus, and Neptune to assess acoustic attenuation in their upper atmospheres (see Appendix B). In all three cases, species diffusion contributes only marginally to total attenuation, with viscous processes—particularly bulk viscosity on Uranus and Neptune—dominating across the altitude ranges considered. Detailed thermophysical profiles, attenuation breakdowns, and transport coefficients for these bodies are presented in Appendix B (Figs. 8–13). For Titan, species diffusion accounts for approximately 5% of attenuation in the upper atmosphere, while Uranus and Neptune show similar contributions near the polar radius ($x_3 = 0$ km).

The relatively minor role of species diffusion in these outer solar system atmospheres stems from lower temperatures, weaker vertical composition gradients, and the dominance of single-species regimes at higher altitudes. On Titan, the 5%α contribution occurs near $x_3 = 1850$ km within a narrow region where the Knudsen number $\text{Kn} < 0.1$ and frequencies approach the acoustic cutoff. This altitude coincides with nearly equal concentrations of N_2 and methane (CH_4); above this level, CH_4 dominates, and species diffusion effects decline. Given the variability in vertical composition across these atmospheres, more detailed characterization of species abundances and stratification is necessary to fully evaluate the role of diffusion in acoustic attenuation.

To fully contextualize the role of species diffusion, we compare classical attenuation, $\alpha_{\text{classical}}$, with absorption due to vibrational relaxation effects, $\alpha_{\text{vibrational}}$ (see Fig. 14). For Earth, Venus, and Mars, vibrational relaxation influences attenuation in the lower atmosphere, where polyatomic molecules such as CO_2 and N_2 exhibit active vibrational modes at prevailing temperatures. However, classical attenuation mechanisms dominate above approximately 120 km in all cases studied. This altitude range also corresponds to where species diffusion contributes most strongly, demonstrating its importance in rarefied upper atmospheric conditions. In contrast, for Titan, Uranus, and Neptune, vibrational relaxation effects are negligible across the altitudes considered.

More broadly, these results demonstrate that species diffusion—particularly barodiffusion—can play a significant role in acoustic attenuation, especially in rarefied upper atmospheric regions where vertical gradients in molecular composition are steep and light species are present in appreciable concentrations. Since atmospheric composition and structure vary with factors such as solar activity, seasonal cycles, and local temperature, the influence of species diffusion is expected to exhibit spatial and temporal variability. These findings highlight the importance of incorporating species diffusion into models of acoustic wave propagation, with direct implications for remote sensing, upper atmospheric modeling, and the design of future planetary exploration missions.

V. CONCLUDING REMARKS

This study examines the effect of species diffusion on the propagation of acoustic and acoustic-gravity waves within mixtures of ideal gases, starting from the multicomponent Navier–Stokes equations. The results were applied specifically to quantify attenuation of acoustic waves in the atmospheres of Earth, Venus, Mars, Titan, Uranus, and Neptune. By deriving a dispersion relation based on macroscopic transport equations from kinetic theory, the present analysis provides a theoretical basis to isolate the roles of specific diffusive processes in wave attenuation in multi-component planetary atmospheres. Among the different species diffusion mechanisms, barodiffusion is identified as the primary contributor, while

https://doi.org/10.1121/10.0042249

ordinary diffusion and thermal diffusion have relatively minor effects. The influence of species diffusion is most pronounced in regions where gases with different molecular masses are prevalent, especially in the upper layers of planetary atmospheres. For example, species diffusion accounts for approximately 16% of total absorption in the upper layers of Earth's atmosphere, 17% in Mars' atmosphere, and up to 45% in Venus' atmosphere. In contrast, species diffusion has a more limited impact on Titan, Uranus, and Neptune, where shear and bulk viscosity effects dominate. These findings refine our understanding of wave propagation in rarefied planetary atmospheres and can inform the use and development of acoustic sensing applications, both on Earth and for future exploration of planetary atmospheres. Technical examples of the calculation of diffusion coefficients and the resulting attenuation coefficients are provided in the Supporting Information as an open-source archive.

Future research will address the influence of species diffusion on gravity wave propagation and consider additional processes, such as vibrational relaxation for acoustic propagation in multi-component atmospheres. Furthermore, investigating wave propagation in rarefied gas mixtures, where continuum models are no longer applicable, can provide a basis for coupling of motion across regimes as waves propagate towards the exobase.

ACKNOWLEDGMENTS

Research at Embry-Riddle Aeronautical University was supported under DARPA Cooperative Agreements HR00112120003 and HR00112320043. This work is approved for public release; distribution is unlimited. The content of the information does not necessarily reflect the position or the policy of the government, and no official endorsement should be inferred. Research by R.S. was conducted as part of the LABEX CeLyA (ANR-10-LABX-0060) of Université de Lyon, within the program Investissements d'Avenir (ANR-16-IDEX-0005) managed by the French National Research Agency (ANR). For Open Access, a CC-BY public copyright license has been applied by the authors to the present document and will be applied to all subsequent versions up to the Author Accepted Manuscript arising from this submission.

AUTHOR DECLARATIONS

Conflict of Interest

The authors have no conflicts to disclose.

DATA AVAILABILITY

All digital materials underlying this study, including datasets and analysis scripts, are available in the ERAU Scholarly Commons institutional open-access repository. The materials are archived as a versioned release and are accessible via the following DOI: https://doi.org/10.17632/ygrr6nf635.1.

APPENDIX A: VENUSIAN TRANSPORT COEFFICIENTS

This section presents the Venusian transport coefficients omitted from the main text. They are included here for completeness.

Figure 7 presents transport coefficients for two Venusian atmospheric profiles: V1 [Figs. 7(A)–7(C)] and V2 [Figs. 7(D)–7(F)]. While the compositional profiles differ significantly, the thermoviscous coefficients are nearly identical, except for thermal conductivity. In particular, V2 exhibits thermal conductivities up to 15% higher than V1, especially at higher altitudes.

Species flux coefficients and thermodiffusion ratios show stronger altitude-dependent differences due to compositional variations. For instance, the thermodiffusion ratio of helium in V1 [Fig. 7(C)] remains negative above 150 km and asymptotically approaches zero, whereas in V2 [Fig. 7(F)] it becomes positive with altitude. This behavior reflects the need for thermodiffusion ratios to satisfy the mass constraint defined in Eq. (1e).

The species flux coefficient $C_{46,0}$, representing diffusion between helium and oxygen in the six-species Venusian mixture, follows a similar trend. In both V1 [Fig. 7(B)] and V2 [Fig. 7(E)], $C_{46,0}$ is comparable below 150 km. However, above this altitude, differing He and O abundances lead to a marked decrease in $C_{46,0}$ for V2 around 250 km, while in V1 it continues to rise. These variations directly affect the attenuation expression for species diffusion, as the relevant coefficients appear proportionally.

APPENDIX B: OUTER SOLAR SYSTEM BODIES: TITAN, URANUS, AND NEPTUNE

Beyond the terrestrial planets are the atmospheres of Titan, Uranus, and Neptune, which contain higher concentrations of methane (CH_4) and molecular hydrogen (H_2). Although the attenuation due to species diffusion is relatively small in these atmospheres, their composition significantly influences the role of bulk viscosity, which has previously been a minor contributor to acoustic wave attenuation. In the following, we provide a discussion on the outer solar system bodies. For Uranus and Neptune, an altitude of $x_3 = 0$ km refers to the planetary radius, where pressure is equal to 10^5 Pa.

Table II shows the parameters used for the outer planetary bodies, as obtained from NASA-GRAM suite Justh and Hoffman (2020).

1. Titan

Titan's atmosphere is primarily a binary mixture of N_2 and CH_4, with trace amounts of argon (Ar). It is characterized by photochemical haze, convective storms, and orography capable of generating atmospheric waves (Hörst, 2017).

Figure 8 presents the vertical atmospheric structure of Titan. Figure 8(A) shows that near the surface, Titan's atmosphere consists of 95% N_2, 3.15% Ar, and 1.85% CH_4. This

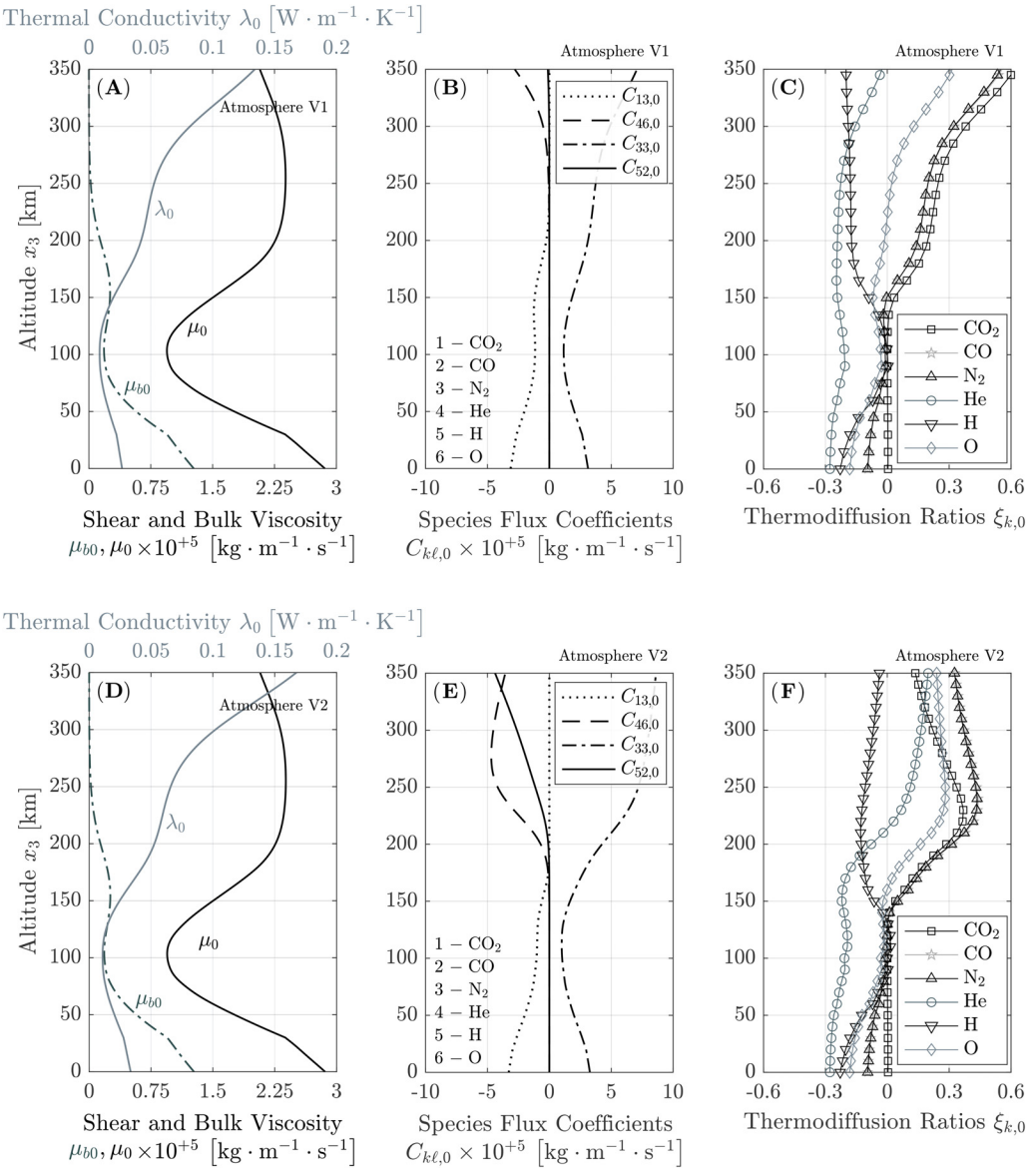

FIG. 7. Transport coefficients for two modeled Venusian atmospheres.

composition remains relatively stable up to 1000 km, at which point CH_4 concentrations increase and N_2 gradually decreases.

Titan's ambient temperature profile in Fig. 8(B) exhibits fluctuations before transitioning to an isothermal state above $x_3 > 800$ km, where $T_0 = 177$ K. The large scale height at the surface, $h_0(x_3 = 0) = 35$ km, leads to a more gradual exponential decay in density and pressure compared to terrestrial planets. As a result, the region where the Knudsen number remains below 0.1 Fig. 8(C) extends to higher altitudes, since $\mathrm{Kn} \propto 1/\rho_0$. Titan also exhibits a notably low acoustic cutoff frequency, with $\omega_a(x_3 = 0)/2\pi = 7.63 \times 10^{-4}$ Hz—approximately one-fourth that of Earth at the same altitude. The maximum cutoff frequency, $f_a = 8.5 \times 10^{-4}$ Hz [outside the range shown in Fig. 8(C)], is the lowest among all planets considered, allowing for the propagation of lower-frequency infrasound than is possible in denser, warmer atmospheres.

TABLE II. Planetary parameters used in the appendix analysis for Titan, Uranus, and Neptune.

Planet	Mass $\mathfrak{M}_{\text{planet}}$[kg]	Radius $\mathfrak{R}_{\text{planet}}$[km]	Atmospheric model	Latitude	Longitude	Ground pressure $p_0(x_3 = 0)$[Pa]
Titan	1.345×10^{23}	2575.5	GRAM	22°N	48°W	1.481×10^5
Uranus	8.681×10^{25}	25 362	GRAM	82°N	48°W	10^5
Neptune	1.024×10^{26}	24 622	GRAM	22°N	48°W	10^5

https://doi.org/10.1121/10.0042249

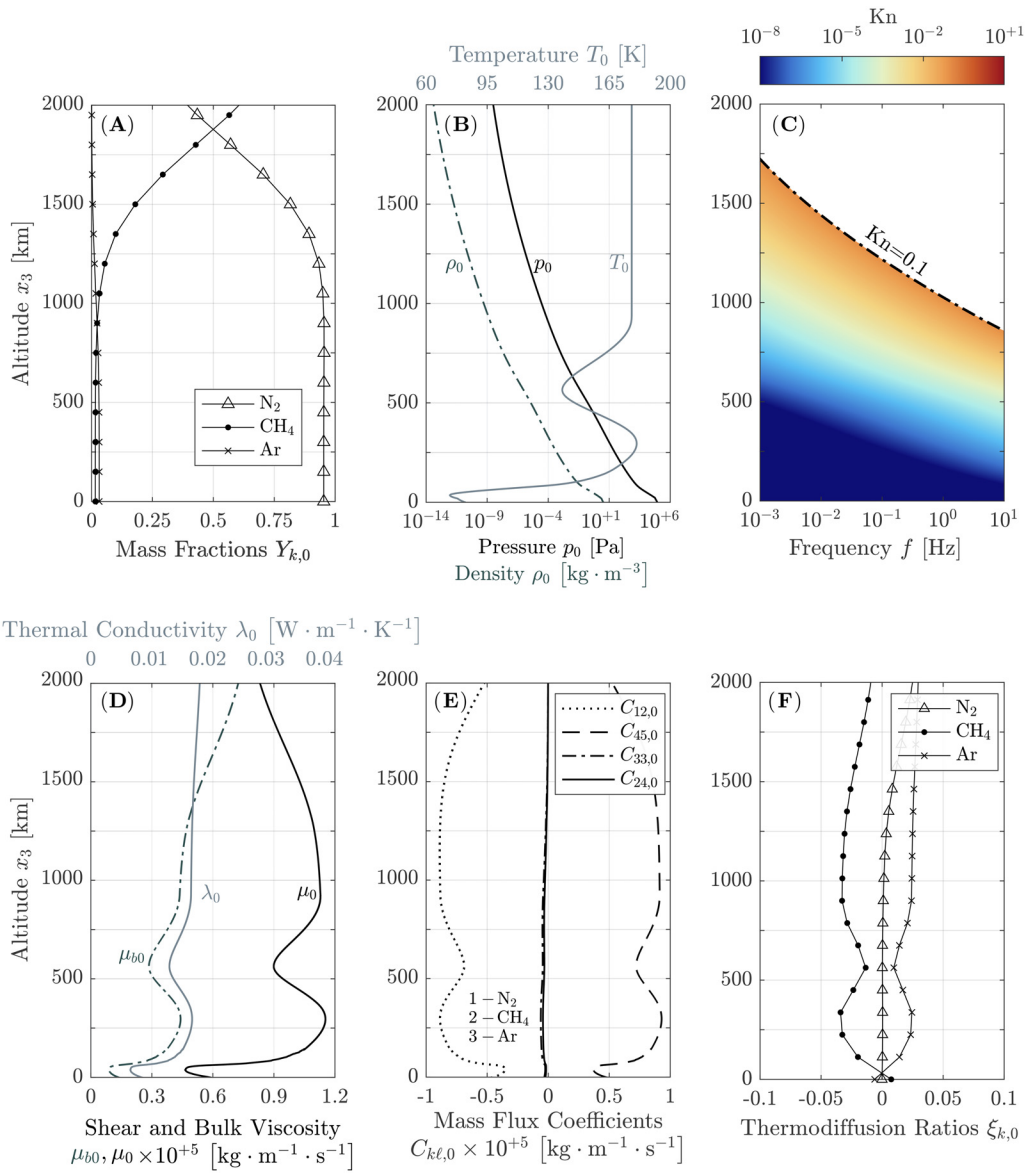

FIG. 8. Estimation of atmospheric conditions on Titan.

The thermoviscous coefficients on Titan [Fig. 8(D)] are of similar magnitude to those of Mars, except for bulk viscosity, which is higher due to the increased concentration of CH_4. The remaining transport coefficients Figs. 8(E)–8(F) remain approximately constant with altitude and are similar in magnitude to those of Mars.

Figure 9 presents the attenuation characteristics of acoustic waves in Titan's atmosphere. Figure 9(A) depicts the attenuation of acoustic waves with varying frequency and altitude on Titan. Acoustic waves experience the least attenuation near Titan's surface compared to the other atmospheres considered in this study. This is due to the combination of low temperatures and relatively high density [$T_0(x_3 = 0) = 80\,\mathrm{K}$ and $\rho_0(x_3 = 0) = 5.72\,\mathrm{kg \cdot m^{-3}}$]. In general, Titan's atmosphere is not strongly dissipative, meaning acoustic waves can propagate vertically for long distances without experiencing significant attenuation. At an altitude of 1000 km and a frequency of $f = 0.01$ Hz, the attenuation on Titan is $\alpha = 0.03$ dB · km^{-1}, which is comparable to the attenuation of acoustic waves on Earth at an altitude of $x_3 = 200$ km.

For $x_3 < 1000$ km, shear viscosity is the dominant mechanism of dissipation, as illustrated in Fig. 9(B). Together, shear viscosity and bulk viscosity account for 60%–70% of the total attenuation coefficient, α, with thermal conductivity contributing next, while species diffusion has a negligible effect. The influence of bulk viscosity follows the compositional profiles [Fig. 8(A)], as CH_4 exhibits a higher bulk viscosity than N_2. At $x_3 = 1875$ km, the dominant species transitions from N_2 to CH_4. The contribution from species diffusion can be predicted using Eq. (28) with equal concentrations of each species $X_{1,0} = X_{2,0} = 0.5$, representing the maximum contribution from species diffusion, approximately $\alpha_{\mathrm{diffusion}} \approx 5\%\alpha$. The contributions from

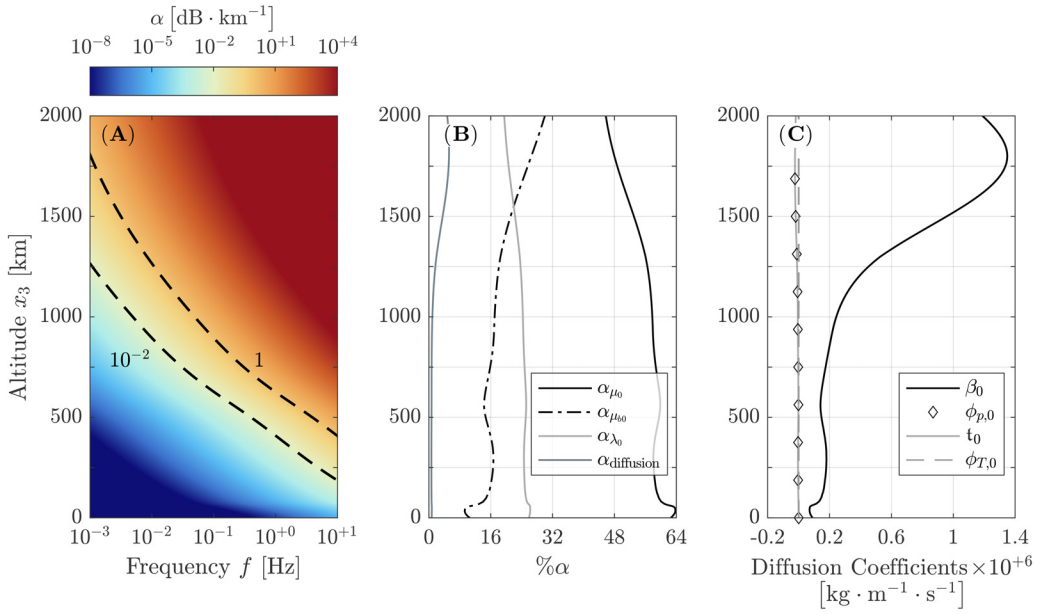

FIG. 9. Attenuation of acoustic waves on Titan.

other transport phenomena are 45%–62% for shear viscosity (α_{μ_0}), 19%–25% for thermal conductivity (α_{λ_0}), and 10%–34% for bulk viscosity (α_{μ_b}).

Although species diffusion contributes ~5% of α in the upper atmosphere, the propagation of acoustic waves is restricted in this region by the Knudsen number, so that frequencies in a narrow bandwidth (1.5×10^{-4} Hz $< f < 5 \times 10^{-4}$ Hz) are valid in this region. The impact of species diffusion could be appreciable under different atmospheric conditions, i.e., a denser or hotter upper atmosphere, which would effectively broaden the region where Kn ≤ 0.1.

2. Uranus

Uranus's atmosphere has been analyzed up to an altitude of 2000 km, where it is composed of approximately 99% hydrogen (H_2). Above 1000 km, the atmosphere approaches a nearly pure H_2 state, rendering species diffusion negligible. As the composition and structure above this altitude resemble a single-component gas, the discussion of acoustic propagation is confined to $x_3 \leq 1000$ km.

Figure 10 presents the atmospheric profiles of Uranus. Figure 10(A) shows the mass fractions $Y_{k,0}$, where the atmosphere is a binary mixture consisting of 75%–99% H_2 and 0–24% He, with trace amounts of CH_4 near the polar radius (not shown) that are negligible. The temperature profile in Fig. 10(B) is approximately linear, increasing at a rate of 0.384 K · km^{-1}. Pressure and density decrease gradually with altitude due to Uranus's large scale height [$h_0(x_3 = 0) = 31.82$ km], which is nearly four times that of Earth. Notably, Uranus's atmosphere exhibits the widest range in which the Knudsen number remains below the continuum threshold (Kn ≤ 0.1), as shown in Fig. 10(C).

The thermoviscous coefficients, shown in Fig. 10(D), follow the temperature profile and are strongly influenced by the H_2-rich composition. Bulk viscosity dominates over shear viscosity, with the bulk-to-shear viscosity ratio increasing from $\mu_{b,0}/\mu_0 = 9.88$ at $x_3 = 66$ km to a peak of $\mu_{b,0}/\mu_0 = 38.9$ at $x_3 = 1000$ km. This contrasts clearly with Earth's atmosphere, where $\mu_{b,0}/\mu_0$ is generally less than 0.6. The mass flux coefficients, shown in Fig. 10(E), and the rescaled thermodiffusion ratios exhibit behavior comparable to the mass diffusivity coefficients observed on Mars.

Figure 11 shows the attenuation characteristics of acoustic waves in Uranus's atmosphere. Figure 11(A) shows the attenuation of acoustic waves with altitude and frequency for Uranus's atmosphere. Uranus's atmosphere is even less dissipative than that of Titan, reaching a value of $\alpha = 6.36 \times 10^{-4}$ dB · km^{-1} at $f = 0.01$ Hz, at 1000 km, almost 50 times less than that of Titan at the same altitude and frequency. The contribution of each transport phenomenon to attenuation is shown in Fig. 11(B), where the mechanism responsible for attenuation of acoustic waves on Uranus is primarily bulk viscosity, which accounts for over 85% of the total dissipation ($\alpha_{\mu_{b,0}} > 85\%\alpha$), while thermal conductivity, shear viscosity, and species diffusion contribute 1%–5%α, 3%–10%α, and 0%–1.9%α, respectively.

The barodiffusion coefficient β_0, shown in Fig. 11(C), increases linearly with temperature below $x_3 = 500$ km. Above this altitude, it decreases as the atmosphere transitions to a single-species H_2 fluid. Since Uranus's atmosphere is a binary mixture, attenuation due to species diffusion can be analyzed using Eq. (28). For example, at $x_3 = 0$, $\rho_0 \mathcal{D}^{\text{bin}}_{\text{H}_2-\text{He}} = 6.34 \times 10^{-6}$ kg · m^{-1} · s^{-1}, and with $Y_{\text{H}_2} = 0.617$, the diffusion contribution to attenuation is $\alpha_{\text{diffusion}} = 1.48\%\alpha$, as shown in Fig. 11(B). Between 0 and 500 km, the concentrations of H_2 and He remain relatively constant, and the barodiffusion coefficient β_0^{bin} increases monotonically with temperature. Above 500 km, as the atmosphere transitions to a single-component H_2 gas, β_0^{bin} decreases. Although the barodiffusion coefficient peaks at

https://doi.org/10.1121/10.0042249

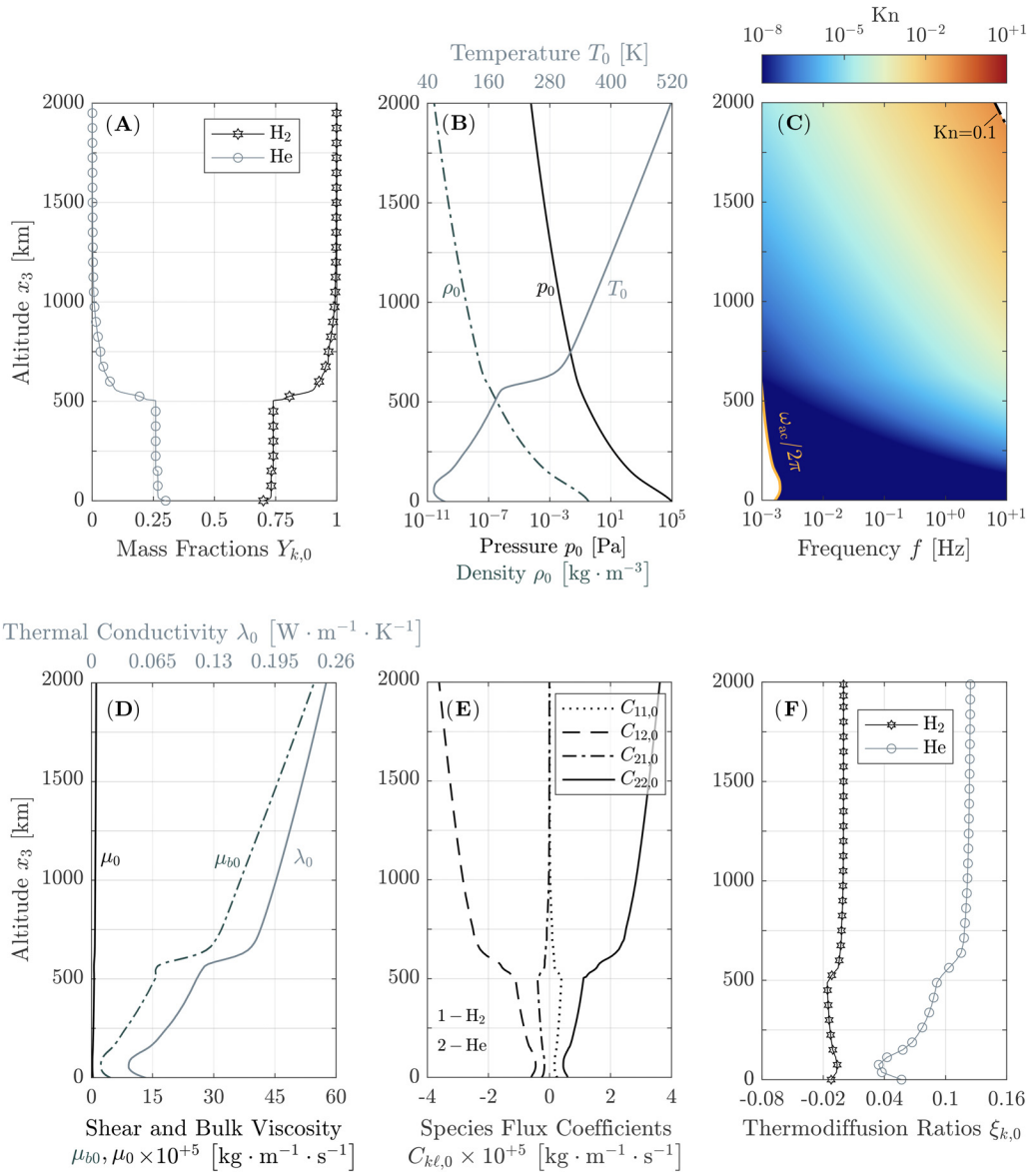

FIG. 10. Estimation of vertical profiles for Uranus's atmosphere.

$x_3 = 500$ km, the thermoviscous coefficients also increase proportionally. At these altitudes, species diffusion contributes only 0.75%α, becoming negligible at higher altitudes as the atmosphere becomes dominated by H_2. Moreover, due to the relatively small molecular mass difference between H_2 and He ($M_{H_2} - M_{He} = 2$ g · mol^{-1}), species diffusion will generally contribute minimally to overall attenuation.

3. Neptune

Neptune's atmosphere shares similarities with that of Uranus in terms of its neutral compositional structure [Fig. 12(A)], as well as its temperature and density profiles [Fig. 12(B)]. Differences arise in Neptune's lower atmosphere, which contains a higher concentration of CH_4, peaking at ∼5% around $x_3 = 50$ km [Fig. 12(A)]. Above 500 km, where the CH_4 concentration drops to nearly zero, the atmospheres of Uranus and Neptune become almost identical—except for the fact that Uranus's atmosphere is approximately 60 times denser than Neptune's. Due to the less dense atmosphere, acoustic propagation is more restricted at higher altitudes compared to Uranus [cf. Fig. 12(C)].

The transport coefficients [cf. Figs. 12(D)–12(F)] are of similar magnitude to those in Uranus's atmosphere. The ratio $\mu_{b,0}/\mu_0 = 35.65$ at $x_3 = 1000$ km, which is comparable to that of Uranus. This ratio continues to increase with temperature, reaching a maximum value of $\mu_{b,0}/\mu = 46$ at $x_3 = 2000$ km. The rescaled thermodiffusion ratio profile for CH_4 reaches the highest value for any gas in this study, $\xi_{3,0}(x_3 > 1000\ \text{km}) \approx 0.6$. However, this ratio does not significantly impact the total attenuation of the wave since the concentration of CH_4 is approximately nil at those altitudes.

Figure 13 shows the attenuation properties of acoustic waves in Neptune's atmosphere. Figure 13(A) shows the attenuation coefficient for Neptune's atmosphere. Since Neptune's atmosphere is less dense, it is more dissipative than

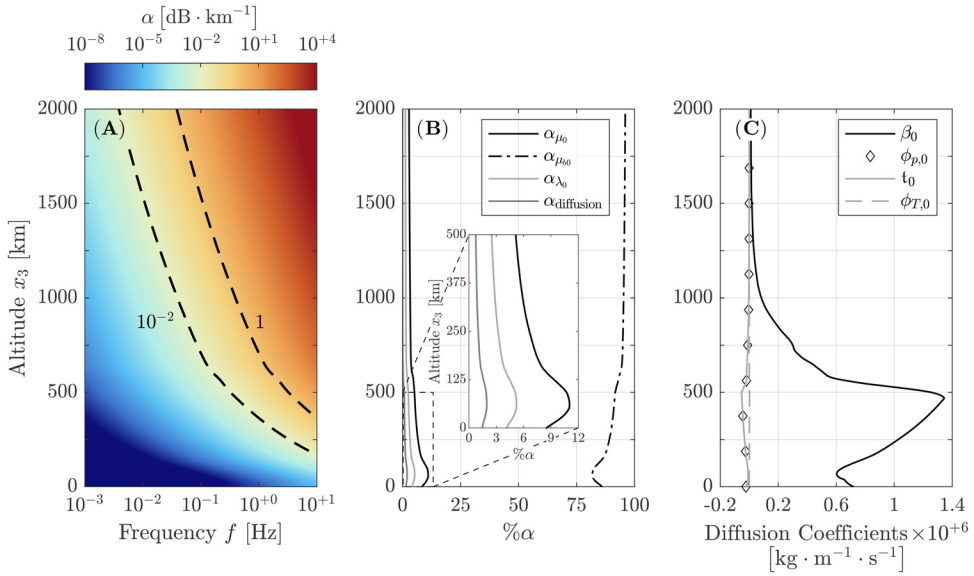

FIG. 11. Attenuation of acoustic waves in Uranus's atmosphere.

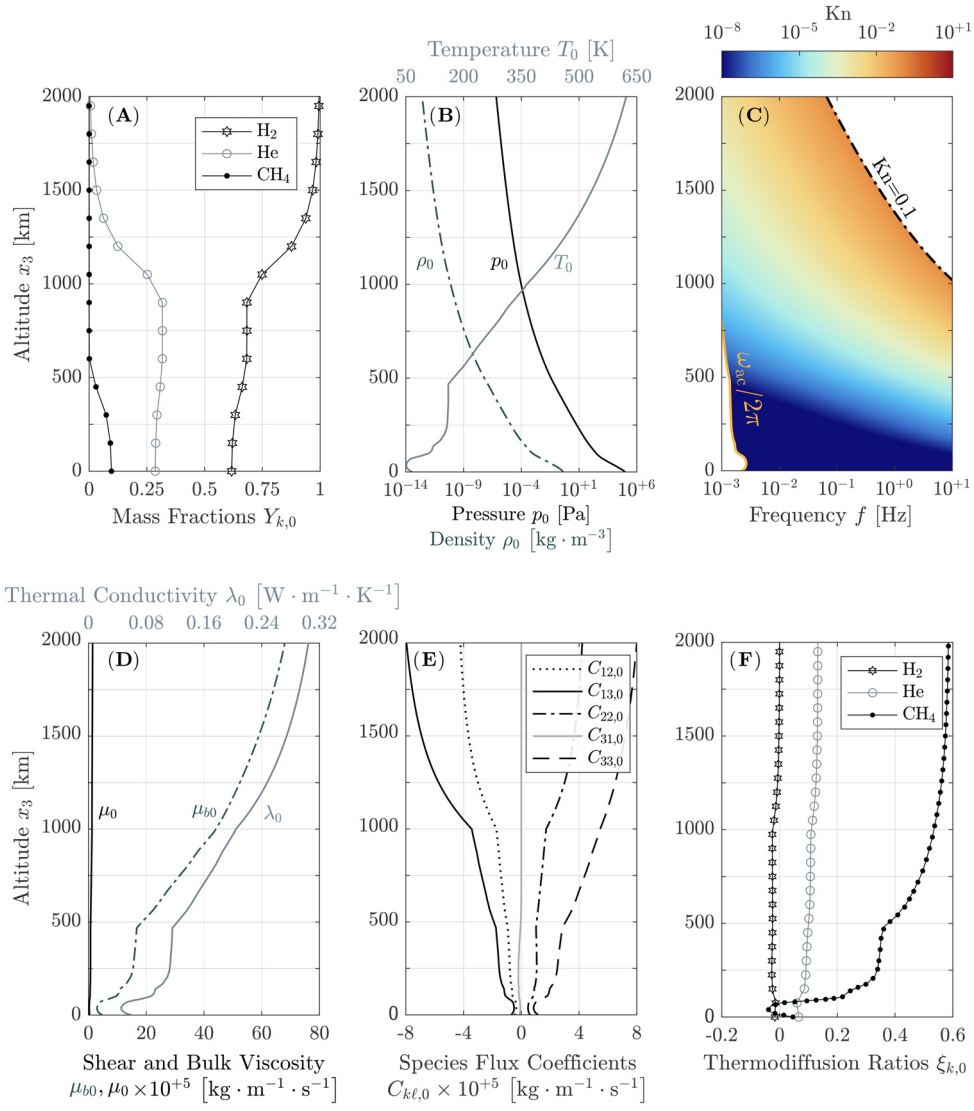

FIG. 12. Estimations of vertical profiles for Neptune's atmosphere.

https://doi.org/10.1121/10.0042249

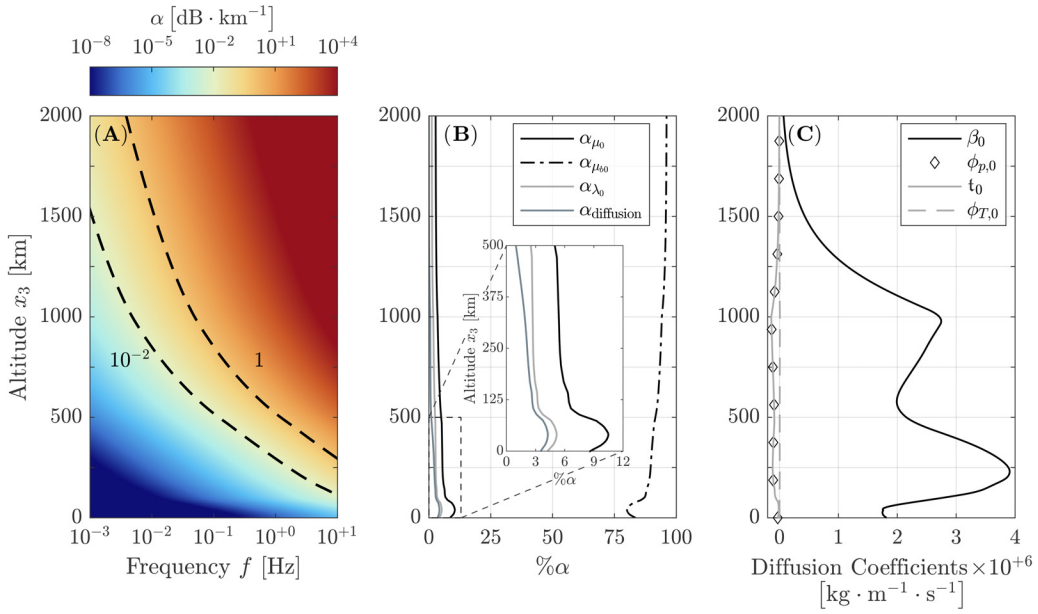

FIG. 13. Attenuation of acoustic waves in Neptune's atmosphere.

Uranus's. At 1000 km, for $f = 0.01$ Hz, $\alpha = 0.04$ dB · km^{-1}, which is comparable to attenuation on Titan at the same altitude and frequency. Figure 13(B) shows the individual contributions of each transport phenomenon. Similar to Uranus's atmosphere, bulk viscosity dominates as the primary mechanism of absorption, reaching a maximum of 96% in the upper atmosphere. The contributions of other transport phenomena are minor or negligible, with species diffusion contributing 0%–10.5%, thermal conductivity at 5%, and shear viscosity at 10.5%. Species diffusion contributes the most in the lower atmosphere, where the attenuation of acoustic waves is low, i.e., $\alpha \sim 10^{-11}$ dB · km^{-1}. Similar to other atmospheres in this study, barodiffusion is the main contributor to species diffusion, as shown in Fig. 13(C). Here, the barodiffusion coefficient is larger than that of Uranus due to the presence of CH_4. However, the species diffusion coefficients are, in general, overshadowed by the significant magnitude of the bulk viscosity coefficient, which increases with the presence of CH_4 and H_2. In general, for both Uranus's and Neptune's atmospheres, the total attenuation can be approximated by the viscous contribution, i.e., $\alpha \approx \alpha_{\mu_{b,0}} + \alpha_{\mu_0}$.

Across Titan, Uranus, and Neptune, species diffusion was consistently found to contribute less than 6%α—often less—under the atmospheric conditions modeled. In all cases, viscous dissipation is dominant, with bulk viscosity playing the primary role on Uranus and Neptune, driven by the presence of CH_4 and H_2. While species diffusion had a relatively minor effect, it is sensitive to vertical gradients in composition. A more complete understanding of the compositional structure, particularly at higher altitudes, would allow for improved assessment of its role in acoustic attenuation on these outer solar system bodies.

APPENDIX C: ON THE RELATIVE IMPORTANCE OF CLASSICAL ABSORPTION AND VIBRATIONAL RELAXATION

Vibrational relaxation is widely recognized to play a major role in acoustic wave attenuation in planetary atmospheres (Garcia *et al.*, 2017; Bass *et al.*, 1984; Bauer, 1972; Bass and Chambers, 2001; Gillier *et al.*, 2024; Petculescu and Lueptow, 2007; Sabatini *et al.*, 2016a; Sutherland and Bass, 2004; Trahan and Petculescu, 2020). While a rigorous derivation of its contribution is beyond the scope of this paper, estimating its impact is essential for assessing the significance of the present results.

To estimate this contribution, we apply the methodology outlined in Gillier *et al.* (2024) to compute the vibrational relaxation attenuation coefficient, $\alpha_{\text{vibrational}}$, and compare it with the Stokes-Kirchhoff attenuation, $\alpha_{\text{classical}}$, where

$$\alpha_{\text{classical}} = \alpha_{\mu_0} + \alpha_{\mu_{b,0}} + \alpha_{\lambda_0}, \tag{C1}$$

with each term defined in Eqs. (27b)–(27d).

Figure 14 shows the total attenuation coefficient, defined as $\alpha_{\text{total}} = \alpha + \alpha_{\text{vibrational}}$, plotted versus altitude (x_3) and frequency (f) for Earth, Mars, and the two Venusian atmospheres (V1 and V2). The dashed black line in each figure identifies the altitude where absorption due to vibrational relaxation is equal to the classical attenuation coefficient, i.e., $\alpha_{\text{vibrational}} = \alpha_{\text{classical}}$.

The results reveal that vibrational relaxation dominates acoustic attenuation in the lower atmosphere—where species diffusion is minimal—across Earth, Mars, and Venus, with a significant contribution below approximately 120 km.

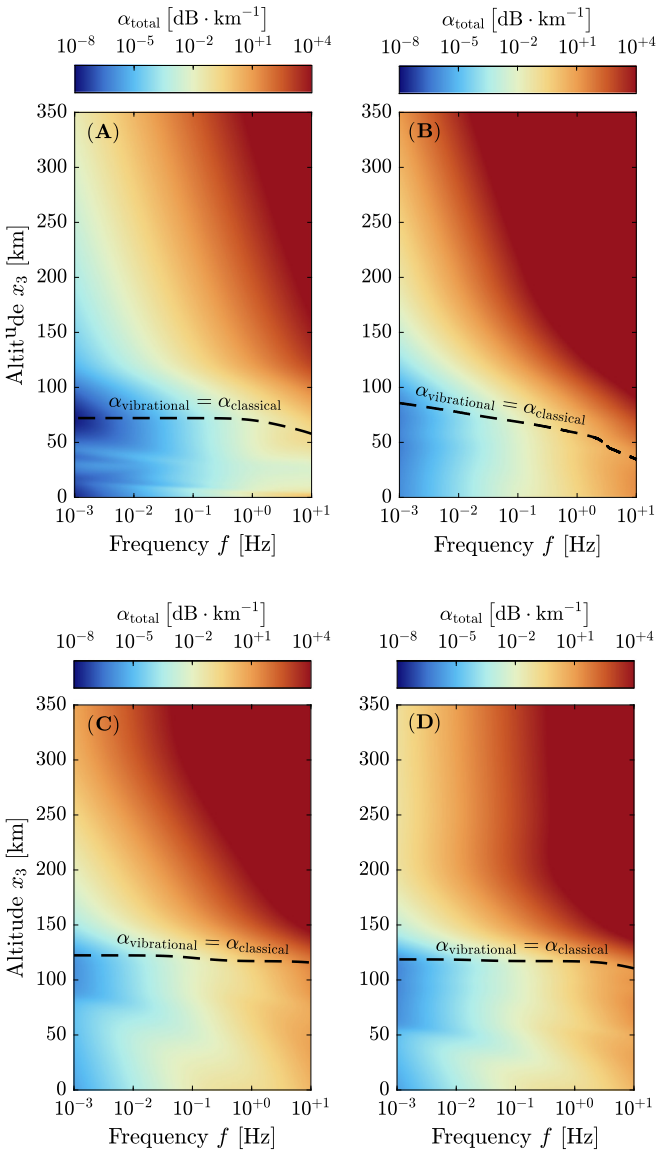

FIG. 14. The total attenuation coefficient α_{total} as a function of altitude x_3 and frequency f for (A) Earth, (B) Mars, (C) Venus Atmosphere V1, and (D) Venus Atmosphere V2.

Conversely, at higher altitudes, attenuation is primarily controlled by viscous stresses, thermal conduction, and species diffusion.

We also analyzed the vibrational relaxation contribution in Titan, Uranus, and Neptune (profiles not included). In these atmospheres, vibrational relaxation remains subdominant over the entire altitude range considered; that is, $\alpha_{\text{vibrational}}$ never exceeds the classical attenuation coefficient. This behavior is attributed to the relatively low atmospheric temperatures, which are insufficient to significantly excite the vibrational modes of the dominant molecular species.

In the upper atmospheres of Venus, Mars, and Earth, vibrational relaxation becomes less important, even in the continued presence of polyatomic species such as CO_2 and N_2. This reduction in contribution arises from a combination of factors. First, upper atmospheres are generally cooler, and although vibrational relaxation is sensitive to temperature, the vibrational temperatures of the relevant molecular modes are on the order of several thousand kelvin, rendering them effectively inactive under typical conditions. Second, the atmosphere becomes increasingly rarefied with altitude, which reduces the collision frequency and increases the relaxation time, further limiting energy exchange. Finally, compositional changes at high altitudes—especially the decline in polyatomic species with accessible vibrational modes—reduce the availability of molecules capable of participating in vibrational relaxation. Together, these effects suppress vibrational energy exchange, making vibrational relaxation negligible relative to classical mechanisms.

APPENDIX D: TRANSPORT COEFFICIENTS

Z_k^{int}	Collision numbers
$\psi_{k\ell}$	Lennard-Jones Potential
$\sigma_{k\ell}$	Collision diameter of $k-\ell$ pair
ϵ_k	Potential Well Depth of the kth species
d	Particle hard-shell diameter of the mixture
$\mathfrak{c}$	Specific heat capacity per molecule
$\mathfrak{m}_k$	molecular mass of the kth species
$\Omega_{k\ell}^{(i,j)}, \Omega_{k\ell}^{(i,j)\star}$	Collision integrals, Reduced Collision integrals
$\bar{A}_{k\ell}, \bar{B}_{k\ell}, \bar{C}_{k\ell}$	Ratios of the reduced collision integrals
μ	Shear viscosity
μ_b	Bulk viscosity
$C_{k\ell}$	Multi-component flux coefficient
$D_{k\ell}$	Multi-component diffusion coefficient
λ	Thermal conductivity
ξ_k	Rescaled Thermodiffusion coefficient
$\mathcal{D}_{k\ell}^{\text{bin}}, \mathcal{D}_{k\text{int},\ell}^{\text{bin}}$	Binary diffusion coefficient, Diffusion coefficient for internal energy

The computation of the transport fluxes $\mathcal{F}_k$, $\mathbb{T}$, and $\mathcal{Q}$ requires determining the transport coefficients μ, μ_b, λ, $C_{k\ell}$, $k, \ell \in S$, and ξ_k, $k \in S$. These coefficients are obtained by solving linear systems derived from the kinetic theory of gases. In the work reported in this article, the approach described in Ern and Giovangigli (1994) is used. The Knudsen number is used to characterize the flow regime and determine when the transport coefficients are applicable. It is defined as follows:

$$\text{Kn} = \frac{\ell_{\text{fp}}}{\mathcal{L}} = \left[\frac{k_B T}{\sqrt{2}\pi d^2 p}\right]\frac{f}{c},$$

where the mean free path ℓ_{fp} is defined by the terms in brackets with $d \sim \times 10^{-10}$ m as the effective particle-hard-shell diameter of the mixture. For clarity, the necessary parameters are first defined in the following paragraph.

1. Parameters for pure species and binary mixtures

The calculation of the transport coefficients relies on molecular parameters linked to the interaction potential $\varphi_{k\ell}$

https://doi.org/10.1121/10.0042249

between molecule pairs (k,ℓ), $k,\ell \in S$. In this work, the Lennard–Jones interaction potentials are employed,

$$\varphi_{k\ell}(r) = 4\epsilon_{k\ell}\left\{\left(\frac{\sigma_{k\ell}}{r}\right)^{12} - \left(\frac{\sigma_{k\ell}}{r}\right)^{6}\right\}. \tag{D1}$$

In Eq. (D1), $\sigma_{k\ell}$ denotes the collision diameter, $\epsilon_{k\ell}$ is the potential well depth, and r represents the distance between the molecules. The molecular parameters for species pairs $\epsilon_{k\ell}$ and $\sigma_{k\ell}$ are expressed in terms of the pure species parameters ϵ_k and σ_k as

$$\frac{\epsilon_{k\ell}}{k_B} = \sqrt{\frac{\epsilon_k}{k_B}\frac{\epsilon_\ell}{k_B}}, \quad \sigma_{k\ell} = \frac{\sigma_k + \sigma_\ell}{2}, \tag{D2}$$

where k_B is the Boltzmann constant.

Some transport coefficients depend on the collision numbers Z_k^{int}, $k \in S_{\text{pol}}$, which are associated with the relaxation of internal degrees of freedom. When the energy can be split into independent rotational and vibrational modes, these numbers can be estimated from

$$\frac{\mathfrak{c}_k^{\text{int}}}{Z_k^{\text{int}}} = \frac{\mathfrak{c}_k^{\text{rot}}}{Z_k^{\text{rot}}} + \frac{\mathfrak{c}_k^{\text{vib}}}{Z_k^{\text{vib}}},$$

where Z_k^{rot}, Z_k^{vib} are the rotational and vibrational collision numbers, respectively. The specific heat per molecule of internal energy, $\mathfrak{c}_k^{\text{int}}$, is expressed as

$$\mathfrak{c}_k^{\text{int}} = \mathfrak{c}_{pk} - \mathfrak{c}_p^{\text{tr}}, \tag{D3}$$

where $\mathfrak{c}_p^{\text{tr}} = 5k_B/2$ represents the translational specific heat at constant pressure per molecule and

$$\mathfrak{c}_{pk} = c_{pk}\mathfrak{m}_k, \quad \mathfrak{m}_k = \frac{M_k}{N_A}, \tag{D4}$$

where $\mathfrak{m}_k$ is the molecular mass of species k, N_A is Avogadro's number, and $\mathfrak{c}_{pk}$ denotes the specific heat at constant pressure per molecule of the kth species. Equation (D3) can also be written in terms of $\mathfrak{c}_{vk} = c_{vk}\mathfrak{m}_k$ as $\mathfrak{c}_k^{\text{int}} = \mathfrak{c}_{vk} - \mathfrak{c}_v^{\text{tr}}$ with $\mathfrak{c}_v^{\text{tr}} = 3k_B/2$. The specific heats of the kth species c_{pk} and c_{vk} are determined using the following expressions:

$$c_{pk} = \left[\frac{N_{\text{dof}} + 2}{2}\right]\frac{R}{M_k}, \quad c_{vk} = c_{pk} - \frac{R}{M_k}. \tag{D5}$$

Vibrational relaxation is often addressed using an ad-hoc approach, and only rotational relaxation is included in Z_k^{int}, $Z_k^{\text{int}} = Z_k^{\text{rot}}$. A common approximation for the rotational relaxation numbers is the model by Parker (1959) (see also Brau and Jonkman, 1970),

$$Z_k^{\text{rot}}(T) = Z_k^{\text{rot}}(T = 298\text{K})\frac{F_k(T = 298\text{K})}{F_k(T)},$$

where

TABLE III. Molecular parameters obtained from Ern and Giovangigli (1994), Weaver and Alexeenko (2015) (for He and Ar), Capitelli *et al.* (2000) (for N).

Species	M_k [g · mol^{-1}]	ϵ_k/k_B [K]	σ_k [Å]	$Z_k^{\text{rot}}(T = 298\text{K})$
CH_4	16.04	141.4	3.746	13.0
CO	28.01	98.1	3.650	1.8
CO_2	44.01	244.0	3.763	2.1
H	1.008	145.0	2.050	—
H_2	2.016	38.0	2.920	280.0
N_2	28.013	97.5	3.621	4.0
N	14.007	119.2	2.980	—
O	16	80.0	2.750	—
O_2	32	107.4	3.458	3.8
He	4.003	10.2	2.524	—
Ar	39.948	143.8	3.323	—

$$F_k(T) = 1 + \frac{\pi^{3/2}}{2}\left(\frac{\epsilon_k/k_B}{T}\right)^{1/2} + \left(\frac{\pi^2}{4} + 2\right)\frac{\epsilon_k/k_B}{T}.$$

The collision diameters σ_k, potential well depths ϵ_k/k_B, and collision numbers $Z_k^{\text{rot}}(T = 298\text{K})$ for the various species considered in this work are presented in Table III, along with their respective molar masses.

The transport coefficients also depend on the so-called reduced collision integrals, $\Omega_{k\ell}^{(i,j)\star}$, which are functions of the reduced temperature $T^\star = T/(\epsilon_{k\ell}/k_B)$. These integrals are obtained by interpolating the data provided in Appendix B from Kim and Monroe (2014). The rescaled collision integrals $\Omega_{k\ell}^{(i,j)\star}$ are related to the collision integrals $\Omega_{k\ell}^{(i,j)}$ via the expression

$$\Omega_{k\ell}^{(i,j)} = \Omega_{k\ell}^{(i,j)\star}\left[\left(\frac{k_B T\pi}{2\mathfrak{m}_{k\ell}}\right)^{1/2}\frac{(j+1)!}{2}\left(1 - \frac{1 + (-1)^i}{2(i+1)}\right)\sigma_{k\ell}^2\right],$$

where

$$\mathfrak{m}_{k\ell} = \mathfrak{m}_{\ell k} = \frac{\mathfrak{m}_k\mathfrak{m}_\ell}{\mathfrak{m}_k + \mathfrak{m}_\ell} \tag{D6}$$

is the reduced mass of the species pair (k,ℓ), $k,\ell \in S$. Additionally, three ratios of the reduced collision integrals, $\overline{A}_{k\ell}$, $\overline{B}_{k\ell}$, and $\overline{C}_{k\ell}$, arise in the transport coefficients and are defined as follows:

$$\overline{A}_{k\ell} = \frac{\Omega_{k\ell}^{(2,2)\star}}{\Omega_{k\ell}^{(1,1)\star}}, \quad \overline{B}_{k\ell} = \frac{5\Omega_{k\ell}^{(1,2)\star} - 4\Omega_{k\ell}^{(1,3)\star}}{\Omega_{k\ell}^{(1,1)\star}}, \quad \overline{C}_{k\ell} = \frac{\Omega_{k\ell}^{(1,2)\star}}{\Omega_{k\ell}^{(1,1)\star}}. \tag{D7}$$

The shear viscosity for a pure species, μ_k, and for a binary species, $\mu_{k\ell}$, are provided by the expressions

$$\mu_k = \frac{5}{16}\frac{\sqrt{\pi\mathfrak{m}_k k_B T}}{\pi\sigma_k^2\Omega_{kk}^{(2,2)*}}, \quad \mu_{k\ell} = \frac{5}{16}\frac{\sqrt{2\pi\mathfrak{m}_{k\ell} k_B T}}{\pi\sigma_{k\ell}^2\Omega_{k\ell}^{(2,2)*}}. \tag{D8}$$

The bulk viscosity is nil for a monoatomic species. For a pure polyatomic species k, it is provided by the following expression:

$$\mu_{bk} = \frac{k_B \pi}{4}\left(\frac{\mathfrak{c}_k^{\text{int}}}{\mathfrak{c}_{vk}}\right)^2 \frac{Z_k^{\text{int}}}{\mathfrak{c}_k^{\text{int}}}\mu_k.$$

Finally, the binary diffusion coefficient $\mathcal{D}_{k\ell}^{\text{bin}}$ of the species pair (k,ℓ) is finally given by the following formula:

$$\mathcal{D}_{k\ell}^{\text{bin}} = \mathcal{D}_{\ell k}^{\text{bin}} = \frac{3}{16}\frac{\sqrt{2\pi k_B^3 T^3/\mathfrak{m}_{k\ell}}}{\pi p \sigma_{k\ell}^2 \Omega_{k\ell}^{(1,1)*}}.$$

2. Shear viscosity μ

The shear viscosity μ of a multi-component mixture is calculated via the following weighted sum:

$$\mu = \sum_{k\in S} X_k, \alpha_k^{(\mu)}. \tag{D9}$$

The vector $a^{(\mu)}$ is the solution of the invertible transport linear system

$$H\alpha^{(\mu)} = \beta^{(\mu)}, \tag{D10}$$

where the components of the matrix H and the vector $\beta^{(\mu)}$ are defined as

$$\begin{aligned}
H_{kk} &= \sum_{\substack{\ell\in S\\ \ell\neq k}} \frac{2X_\ell}{\mu_{k\ell}}\left[\frac{5}{3\overline{A}_{k\ell}}\frac{\mathfrak{m}_k\mathfrak{m}_\ell}{(\mathfrak{m}_k+\mathfrak{m}_\ell)^2} + \frac{\mathfrak{m}_\ell^2}{(\mathfrak{m}_k+\mathfrak{m}_\ell)^2}\right] + \frac{X_k}{\mu_k},\\
H_{k\ell} &= \frac{2X_\ell}{\mu_{k\ell}}\frac{\mathfrak{m}_k\mathfrak{m}_\ell}{(\mathfrak{m}_k+\mathfrak{m}_\ell)^2}\left[1-\frac{5}{3\overline{A}_{k\ell}}\right], \quad k\neq\ell,\\
\beta_k^{(\mu)} &= 1, \quad k\in S.
\end{aligned} \tag{D11}$$

3. Bulk viscosity μ_b

The bulk viscosity of a multi-component mixture is determined using the expression

$$\mu_b = \sum_{k\in S_{\text{pol}}}\left(\frac{\mathfrak{c}_{vk}}{\mathfrak{c}_v}\right)^2 \frac{\Omega_{kk}^{(2,2)}X_k}{\sum_{\ell\in S}\Omega_{k\ell}^{(2,2)}X_\ell}\mu_{bk},$$

where the weighted sum is taken over the polyatomic species ($S_{\text{pol}} \subseteq S$).

4. Thermal conductivity λ

The thermal conductivity of a multi-component mixture is given by

$$\lambda = \frac{p}{T}\sum_{k\in S}\alpha_k^{(\lambda)}\beta_k^{(\lambda)}. \tag{D12}$$

The vector $\alpha^{(\lambda)}$ is the solution of the linear system $\hat{\Lambda}\alpha^{(\lambda)} = \hat{\beta}^{(\lambda)}$, where the components of the matrix $\hat{\Lambda}$ and the vector $\beta^{(\lambda)}$ are defined as

$$\hat{\Lambda}_{kk} = \frac{X_k}{\mathcal{D}_{kk}^{\text{bin}}}\left[2\overline{A}_{kk} + \frac{16\overline{A}_{kk}}{15\pi k_B}\frac{\mathfrak{c}_k^{\text{int}}}{Z_k^{\text{rot}}} + \frac{c_k^{\text{int}}}{k_B}\frac{\mathcal{D}_{kk}^{\text{bin}}}{\mathcal{D}_{k\text{int},k}^{\text{bin}}}\right] \tag{D13}$$

$$+ \sum_{\substack{\ell\in S\\ \ell\neq k}}\frac{X_\ell}{\mathcal{D}_{k\ell}^{\text{bin}}}\frac{\mathfrak{m}_k\mathfrak{m}_\ell}{(\mathfrak{m}_k+\mathfrak{m}_\ell)^2}\Xi_{k\ell}, \quad k\in S, \tag{D14}$$

$$\hat{\Lambda}_{k\ell} = -\frac{X_\ell}{\mathcal{D}_{k\ell}^{\text{bin}}}\frac{\mathfrak{m}_k\mathfrak{m}_\ell}{(\mathfrak{m}_k+\mathfrak{m}_\ell)^2}\Psi_{k\ell}, \tag{D15}$$

$$\tilde{\beta}_k^{(\lambda)} = \frac{\mathfrak{c}_p^{\text{tr}} + \mathfrak{c}_k^{\text{int}}}{k_B}, \tag{D16}$$

$$\beta_k^{(\lambda)} = X_k\tilde{\beta}_k^{(\lambda)}, \tag{D17}$$

with

$$\begin{aligned}
\Xi_{k\ell} &= \frac{15}{2}\frac{\mathfrak{m}_k}{\mathfrak{m}_\ell} + \left[\frac{25}{4} - 3\overline{B}_{k\ell}\right]\frac{\mathfrak{m}_\ell}{\mathfrak{m}_k} + 4\overline{A}_{k\ell}\\
&\quad + \frac{4}{15}\frac{(3\mathfrak{m}_k - 2\mathfrak{m}_\ell)^2}{\mathfrak{m}_\ell^2}\frac{\overline{A}_{k\ell}}{\pi k_B}\frac{\mathfrak{c}_k^{\text{int}}}{Z_k^{\text{int}}} + \frac{20}{3}\frac{\overline{A}_{k\ell}}{\pi k_B}\frac{\mathfrak{c}_\ell^{\text{int}}}{Z_\ell^{\text{int}}}\\
&\quad + \frac{(\mathfrak{m}_k+\mathfrak{m}_\ell)^2}{\mathfrak{m}_k\mathfrak{m}_\ell}\frac{\mathfrak{c}_k^{\text{int}}}{k_B},\\
\Psi_{k\ell} &= \frac{55}{4} - 3\overline{B}_{k\ell} - 4\overline{A}_{k\ell} + \frac{4}{3}\frac{\overline{A}_{k\ell}}{\pi k_B}\frac{3\mathfrak{m}_k - 2\mathfrak{m}_\ell}{\mathfrak{m}_\ell}\frac{\mathfrak{c}_k^{\text{int}}}{Z_k^{\text{int}}}\\
&\quad + \frac{4}{3}\frac{\overline{A}_{k\ell}}{\pi k_B}\frac{3\mathfrak{m}_\ell - 2\mathfrak{m}_k}{\mathfrak{m}_k}\frac{\mathfrak{c}_\ell^{\text{int}}}{Z_\ell^{\text{int}}},
\end{aligned} \tag{D18}$$

where $D_{k,\text{int},\ell}^{\text{bin}} = D_{k\ell}^{\text{bin}}$ can be used for nonpolar gases (Monchick *et al.*, 1965).

5. Multi-component flux coefficient $C_{k\ell}$ and rescaled thermal diffusion ratios ξ_k

The multi-component flux diffusion coefficients $C_{k\ell}$, with $k,\ell\in S$, are the elements of the matrix

$$\mathfrak{C} = \left(\frac{1}{a}\mathcal{Y}\mathbf{1}^T + \Gamma\right)^{-1} - a\left(\mathcal{Y}\mathbf{1}^T\right), \tag{D19}$$

where a is any positive real number, $\mathcal{Y} = [Y_1, Y_2, \ldots, Y_{n_s}]^T$ is the vector of mass fractions, $\mathbf{1} = [1,\ldots,1]^T$ is a vector containing n_s ones, and Γ is the singular matrix whose elements are provided by the following expressions:

$$\begin{aligned}
\Gamma_{kk} &= \sum_{\substack{\ell\in S\\ \ell\neq k}}\frac{M}{M_k}\frac{X_\ell}{\rho\mathcal{D}_{k\ell}^{\text{bin}}}, \quad k\in S,\\
\Gamma_{k\ell} &= -\frac{M}{M_\ell}\frac{X_k}{\rho\mathcal{D}_{k\ell}^{\text{bin}}}, \quad k,\ell\in S, \quad k\neq\ell.
\end{aligned} \tag{D20}$$

The rescaled thermal diffusion ratios ξ_k, $k\in S$ are determined by the formula

$$\xi_k = \sum_{\ell\in S}\tilde{\Omega}_{k\ell}\alpha_\ell^{(\lambda)}, k\in S, \tag{D21}$$

https://doi.org/10.1121/10.0042249

where

$$\tilde{\mathfrak{Q}}_{kk} = -\sum_{\substack{\ell \in S \\ \ell \neq k}} \frac{X_\ell}{2\mathcal{D}^{\text{bin}}_{k\ell}} \frac{\mathfrak{m}_\ell}{\mathfrak{m}_k + \mathfrak{m}_\ell}(6\overline{C}_{k\ell} - 5), \quad k \in S,$$

$$\tilde{\mathfrak{Q}}_{k\ell} = \frac{X_\ell}{2\mathcal{D}^{\text{bin}}_{k\ell}} \frac{\mathfrak{m}_k}{\mathfrak{m}_k + \mathfrak{m}_\ell}(6\overline{C}_{k\ell} - 5), \quad k, \ell \in S, k \neq \ell. \tag{D22}$$

It can be demonstrated that the multi-component diffusion flux coefficients and the rescaled thermal diffusion ratios are constructed to satisfy the mass conservation constraint,

$$\sum_{k \in S} \mathcal{F}_k = 0. \tag{D23}$$

In particular, the matrix $\mathfrak{C}$ verifies the following relations:

$$\mathfrak{C}\mathcal{Y} = 0, \quad \mathfrak{C}\Gamma\mathfrak{C} = \mathfrak{C}, \quad \Gamma\mathfrak{C}\Gamma = \Gamma.$$

Moreover, the matrix with components $C_{k\ell}/Y_k$ is symmetric positive semidefinite. Finally, the rescaled thermal diffusion ratios verify the constraint,

$$\sum_{k \in S} X_k \xi_k = 0. \tag{D24}$$

Anile, M., Pantano, P., Russo, G., and Hunter, J. (**1993**). *Ray Methods for Nonlinear Waves in Fluids and Plasmas* (Chapman & Hall/CRC Press, Boca Raton, FL).

Arnault, P., and Guisset, S. (**2022**). "Chapman–Enskog derivation of multicomponent Navier–Stokes equations," Phys. Plasmas **29**(9), 090901.

Averbuch, G., Houston, R., and Petculescu, A. (**2023**). "Seismo-acoustic coupling in the deep atmosphere of Venus," J. Acoust. Soc. Am. **153**(3), 1802–1810.

Averbuch, G., Waxler, R. M., Smets, P. S. M., and Evers, L. G. (**2020**). "Probabilistic inversion for submerged source depth and strength from infrasound observations," J. Acoust. Soc. Am. **147**(2), 1066–1077.

Bass, H. E., and Chambers, J. P. (**2001**). "Absorption of sound in the martian atmosphere," J. Acoust. Soc. Am. **109**(6), 3069–3071.

Bass, H. E., Sutherland, C., Piercy, J., and Evans, L. (**1984**). *Physical Acoustics* (Academic, New York), Chap. 3.

Bauer, H.-J. (**1972**). "Influences of transport mechanisms on sound propagation in gases," Adv. Mol. Relax. Processes **2**(2), 319–376.

Bergmann, P. G. (**1946**). "The wave equation in a medium with a variable index of refraction," J. Acoust. Soc. Am. **17**(4), 329–333.

Blixt, E. M., Näsholm, S. P., Gibbons, S. J., Evers, L. G., Charlton-Perez, A. J., Orsolini, Y. J., and Kvørna, T. (**2019**). "Estimating tropospheric and stratospheric winds using infrasound from explosions," J. Acoust. Soc. Am. **146**(2), 973–982.

Bowman, D. C., Rouse, J. W., Krishnamoorthy, S., and Silber, E. A. (**2022**). "Infrasound direction of arrival determination using a balloon-borne aeroseismometer," JASA Express Lett. **2**(5), 054001.

Bradley, S. (**2007**). *Atmospheric Acoustic Remote Sensing* (CRC Press, Boca Raton, FL).

Brau, C. A., and Jonkman, R. M. (**1970**). "Classical theory of rotational relaxation in diatomic gases," J. Chem. Phys. **52**(2), 477–484.

Brown, E. H., and Hall, F. F., Jr. (**1978**). "Advances in atmospheric acoustics," Rev. Geophys. **16**(1), 47–110, https://doi.org/10.1029/RG016i001p00047.

Capitelli, M., Gorse, C., Longo, S., and Giordano, D. (**2000**). "Collision integrals of high-temperature air species," J. Thermophys. Heat Transfer **14**(2), 259–268.

Chapman, S., and Cowling, T. G. (**1939**). *An Account of the Kinetic Theory of Viscosity, Thermal Conduction, and Diffusion in Gases* (Cambridge University Press, Cambridge, UK).

Chide, B., Blanc-Benon, P., Bertrand, T., Jacob, X., Lasue, J., Lorenz, R. D., Montmessin, F., Murdoch, N., Pla-Garcia, J., Seel, F., Schröder, S., Stott, A. E., de la Torre Juarez, M., and Wiens, R. C. (**2024**). "An acoustic investigation of the near-surface turbulence on Mars," J. Acoust. Soc. Am. **155**(1), 420–435.

Chunchuzov, I., Kulichkov, S., Perepelkin, V., Popov, O., Firstov, P., Assink, J. D., and Marchetti, E. (**2015**). "Study of the wind velocity-layered structure in the stratosphere, mesosphere, and lower thermosphere by using infrasound probing of the atmosphere," JGR Atmos. **120**(17), 8828–8840.

Eckermann, S. D., Ma, J., and Zhu, X. (**2011**). "Scale-dependent infrared radiative damping rates on Mars and their role in the deposition of gravity-wave momentum flux," Icarus **211**(1), 429–442.

Ern, A., and Giovangigli, V. (**1994**). *Multicomponent Transport Algorithms* (Springer-Verlag, Berlin, Germany).

Evans, L., and Sutherland, L. (**1971**). "Absorption of sound in air," J. Acoust. Soc. Am. **49**, 110.

Fedorenko, A., Kryuchkov, E., Cheremnykh, O., and Selivanov, Y. (**2021**). "Dissipation of acoustic–gravity waves in the Earth's thermosphere," J. Atmos. Sol. Terr. Phys. **212**, 105488.

Fritts, D. C, and Alexander, M. J. (**2003**). "Gravity wave dynamics and effects in the middle atmosphere," Rev. Geophys. **41**(1), 1003, https://doi.org/10.1029/2001RG000106.

Froment, M., Xu, Z., Lognonné, P. H., Larmat, C., Garcia, R. F., Drilleau, M., Delbridge, B. G., Spiga, A., Kawamura, T., and Beucler, É. (**2024**). "Inferring the speed of sound and wind in the nighttime Martian boundary layer from impact-generated infrasound," Geophys. Res. Lett. **51**(18), e2024GL109726, https://doi.org/10.1029/2024GL109726.

Garcia, R. F., Brissaud, Q., Rolland, L., Martin, R., Komatitsch, D., Spiga, A., Lognonné, P., and Banerdt, B. (**2017**). "Finite-difference modeling of acoustic and gravity wave propagation in mars atmosphere: Application to infrasounds emitted by meteor impacts," Space Sci. Rev. **211**(1), 547–570.

Garcia, R. F., Klotz, A., Hertzog, A., Martin, R., Gérier, S., Kassarian, E., Bordereau, J., Venel, S., and Mimoun, D. (**2022**). "Infrasound from large earthquakes recorded on a network of balloons in the stratosphere," Geophys. Res. Lett. **49**(15), e2022GL098844, https://doi.org/10.1029/2022gl098844.

Garrett, S. L. (**2020**). *Attenuation of Sound* (Springer International Publishing, Cham, Switzerland), pp. 673–698.

Gerier, S., Garcia, R. F., Martin, R., and Hertzog, A. (**2024**). "Forward modeling of quake's infrasound recorded in the stratosphere on board balloon platforms," Earth. Planets Space **76**(1), 87.

Gillier, M., Petculescu, A., Murdoch, N., Stott, A. E., Gerier, S., Maurice, S., and Mimoun, D. (**2024**). "Geographical, seasonal and diurnal variations of acoustic attenuation, and sound speed in the near-surface martian atmosphere," J. Geophys. Res. Planets **129**(5), e2023JE008257, https://doi.org/10.1029/2023JE008257.

Godin, O. A. (**2014**). "Dissipation of acoustic-gravity waves: An asymptotic approach," J. Acoust. Soc. Am. **136**(6), EL411–EL417.

Gossard, E. E., and Hooke, W. H. (**1975**). *Waves in the Atmosphere* (Elsevier, Amsterdam, the Netherlands).

Heale, C., Walterscheid, R., and Snively, J. (**2018**). "Localization effects on the dissipation of gravity wave packets in the upper mesosphere and lower thermosphere," JGR Atmos. **123**(17), 8915–8935.

Heale, C. J., Snively, J. B., Hickey, M. P., and Ali, C. J. (**2014**). "Thermospheric dissipation of upward propagating gravity wave packets," J. Geophys. Res. Space Phys. **119**(5), 3857–3872, https://doi.org/10.1002/2013ja019387.

Hickey, M. P., Walterscheid, R. L., and Schubert, G. (**2000**). "Gravity wave heating and cooling in jupiter's thermosphere," Icarus **148**(1), 266–281.

Hickey, M. P., Walterscheid, R. L., and Schubert, G. (**2011**). "Gravity wave heating and cooling of the thermosphere: Sensible heat flux and viscous flux of kinetic energy," J. Geophys. Res. Space Phys. **116**(A12), A12326, https://doi.org/10.1029/2011JA016792.

Hickey, M. P., Walterscheid, R. L., and Schubert, G. (**2015**). "A full-wave model for a binary gas thermosphere: Effects of thermal conductivity and viscosity," J. Geophys. Res. Space Phys. **120**(4), 3074–3083, https://doi.org/10.1002/2014JA020583.

Hines, C. (**1977a**). "Relaxational dissipation in atmospheric waves—I. Basic formulation," Planet. Space Sci. **25**(11), 1045–1060.

Hines, C. (**1977b**). "Relaxational dissipation in atmospheric waves— II. Application to Earth's upper atmosphere," Planet. Space Sci. **25**(11), 1061–1074.

Hines, C. O. (**1960**). "Internal atmospheric gravity waves at ionospheric heights," Can. J. Phys. **38**(11), 60–150.
Horn, R. A., and Johnson, C. R. (**1990**). *Matrix Analysis* (Cambridge University Press, Cambridge, UK).
Hörst, S. M. (**2017**). "Titan's atmosphere and climate," J. Geophys. Res. Planets **122**(3), 432–482, https://doi.org/10.1002/2016JE005240.
Inchin, P. A., Heale, C. J., Snively, J. B., and Zettergren, M. D. (**2020**). "The dynamics of nonlinear atmospheric acoustic-gravity waves generated by tsunamis over realistic bathymetry," J. Geophys. Res. Space Phys. **125**(12), e2020JA028309, https://doi.org/10.1029/2020ja028309.
Justh, H., and Hoffman, J. (**2020**). "Titan global reference atmospheric model (Titan-GRAM): User guide," NASA TM–20205006805 (NASA, Washington, DC).
Justus, C. G., James, B. F., and Johnson, D. L. (**1996**). "Mars Global Reference Atmospheric Model (Mars-GRAM 3.34): Programmer's guide," Technical report (NASA Marshall Space Flight Center, Huntsville, AL).
Kim, S. U., and Monroe, C. W. (**2014**). "High-accuracy calculations of sixteen collision integrals for Lennard-Jones (12–6) gases and their interpolation to parameterize neon, argon, and krypton," J. Comput. Phys. **273**, 358–373.
Kirchhoff, G. (**1868**). "Ueber den Einfluss der Wärmeleitung in einem Gase auf die Schallbewegung" ("On the influence of heat conduction in a gas on sound propagation"), Ann. Phys. **210**(6), 177–193.
Kohler, M. (**1941**). "Schallabsorption in mischungen einatomiger gase" ("Sound absorption in mixtures of monatomic gases"), Ann. Phys. **431**(3), 209–225.
Lalande, J.-M., Sêbe, O., Landès, M., Blanc-Benon, P., Matoza, R. S., Le Pichon, A., and Blanc, E. (**2012**). "Infrasound data inversion for atmospheric sounding," Geophys. J. Int. **190**(1), 687–701.
Landau, L. D., and Lifshitz, E. M. (**1987**). *Fluid Mechanics, 6 of Course of Theoretical Physics*, 2nd ed. (Pergamon, Oxford, UK).
Le Pichon, A., Elisabeth, B., and Hauchecorne, A. (**2009**). *Infrasound Monitoring for Atmospheric Studies* (Springer, Dordrecht, the Netherlands).
Markham, J. J., Beyer, R. T., and Lindsay, R. B. (**1951**). "Absorption of sound in fluids," Rev. Mod. Phys. **23**, 353–411.
Martire, L., Garcia, R. F., Rolland, L., Spiga, A., Lognonné, P. H., Banfield, D., Banerdt, W. B., and Martin, R. (**2020**). "Martian infrasound: Numerical modeling and analysis of insight's data," J. Geophys. Res. Planets **125**(6), e2020JE006376, https://doi.org/10.1029/2020JE006376.
Matoza, R. S., Fee, D., Assink, J. D., Iezzi, A. M., Green, D. N., Kim, K., Toney, L., Lecocq, T., Krishnamoorthy, S., Lalande, J.-M., Nishida, K., Gee, K. L., Haney, M. M., Ortiz, H. D., Brissaud, Q., Martire, L., Rolland, L., Vergados, P., Nippress, A., Park, J., Shani-Kadmiel, S., Witsil, A., Arrowsmith, S., Caudron, C., Watada, S., Perttu, A. B., Taisne, B., Mialle, P., Pichon, A. L., Vergoz, J., Hupe, P., Blom, P. S., Waxler, R., Angelis, S. D., Snively, J. B., Ringler, A. T., Anthony, R. E., Jolly, A. D., Kilgour, G., Averbuch, G., Ripepe, M., Ichihara, M., Arciniega-Ceballos, A., Astafyeva, E., Ceranna, L., Cevuard, S., Che, I.-Y., Negri, R. D., Ebeling, C. W., Evers, L. G., Franco-Marin, L. E., Gabrielson, T. B., Hafner, K., Harrison, R. G., Komjathy, A., Lacanna, G., Lyons, J., Macpherson, K. A., Marchetti, E., McKee, K. F., Mendo-Pérez, G., Mikesell, T. D., Munaibari, E., Oyola-Merced, M., Park, I., Pilger, C., Ramos, C., Ruiz, M. C., Sabatini, R., Schwaiger, H. F., Tailpied, D., Talmadge, C., Vidot, J., Webster, J., and Wilson, D. C. (**2022**). "Atmospheric waves global seismoacoustic observations january 2022 Hunga Eruption, Tonga," Science **377**(6601), 95–100.
Monchick, L., Pereira, A. N. G., and Mason, E. A. (**1965**). "Heat conductivity of polyatomic and polar gases and gas mixtures," J. Chem. Phys. **42**(9), 3241–3256.
Nozuka, Y., Inchin, P. A., Kaneko, Y., Sabatini, R., and Snively, J. B. (**2024**). "Earthquake source impacts on the generation and propagation of seismic infrasound to the upper atmosphere," Geophys. J. Int. **238**(1), 537–556.
Park, J., Assink, J., Stump, B., Hayward, C., Arrowsmith, S., and Che, I.-Y. (**2022**). "Atmospheric model inversion using infrasound signals from the North Korean underground nuclear explosion and the subsequent collapse event in 2017," Geophys. J. Int. **232**(2), 902–922.
Parker, J. G. (**1959**). "Rotational and vibrational relaxation in diatomic gases," Phys. Fluids **2**(4), 449–462.
Petculescu, A. (**2016**). "Acoustic properties in the low and middle atmospheres of Mars and Venus," J. Acoust. Soc. Am. **140**(2), 1439–1446.
Petculescu, A., and Lueptow, R. M. (**2007**). "Atmospheric acoustics of Titan, Mars, Venus, and Earth," Icarus **186**(2), 413–419.
Picone, J. M., Hedin, A. E., Drob, D. P., and Aikin, A. C. (**2002**). "NRLMSISE-00 empirical model of the atmosphere: Statistical comparisons and scientific issues," J. Geophys. Res. Space Phys. **107**(A12), SIA 15, https://doi.org/10.1029/2002ja009430.
Pierce, A. (**1978**). "Aeroacoustic fluid dynamic equations and their acoustic energy conservation corollary with O_2 and N_2 vibrational relaxation effects included," J. Sound Vib. **58**(2), 189–200.
Pitteway, M. L. V., and Hines, C. O. (**1963**). "The viscous damping of atmospheric gravity waves," Can. J. Phys. **41**(12), 1935–1948.
Richmond, A. (**1978**). "Gravity wave generation, propagation, and dissipation in the thermosphere," J. Geophys. Res. Space Phys. **83**(A9), 4131–4145, https://doi.org/10.1029/JA083iA09p04131.
Sabatini, R., Bailly, C., Marsden, O., and Gainville, O. (**2016a**). "Characterization of absorption and non-linear effects in infrasound propagation using an augmented Burgers' equation," Geophys. J. Int. **207**(3), 1432–1445.
Sabatini, R., Marsden, O., Bailly, C., and Bogey, C. (**2016b**). "A numerical study of nonlinear infrasound propagation in a windy atmosphere," J. Acoust. Soc. Am. **140**(1), 641–656.
Sabatini, R., Snively, J. B., Hickey, M. P., and Garrison, J. L. (**2019**). "An analysis of the atmospheric propagation of underground-explosion-generated infrasonic waves based on the equations of fluid dynamics: Ground recordings," J. Acoust. Soc. Am. **146**(6), 4576–4591.
Stokes, G. G. (**2009**). *On the Theories of the Internal Friction of Fluids in Motion, and of the Equilibrium and Motion of Elastic Solids, Cambridge Library Collection – Mathematics* (Cambridge University Press, Cambridge, UK), pp. 75–129.
Sutherland, L. C., and Bass, H. E. (**2004**). "Atmospheric absorption in the atmosphere up to 160 km," J. Acoust. Soc. Am. **115**(3), 1012–1032.
Trahan, A. J., and Petculescu, A. (**2020**). "Absorption of infrasound in the lower and middle clouds of Venus," J. Acoust. Soc. Am. **148**(1), 141–152.
Vadas, S. L. (**2013**). "Compressible *f*-plane solutions to body forces, heatings, and coolings, and application to the primary and secondary gravity waves generated by a deep convective plume," J. Geophys. Res. Space Phys. **118**(5), 2377–2397, https://doi.org/10.1002/jgra.50163.
Vadas, S. L., and Fritts, D. C. (**2005**). "Thermospheric responses to gravity waves: Influences of increasing viscosity and thermal diffusivity," J. Geophys. Res. **110**(D15), D15103, https://doi.org/10.1029/2004JD005574.
Vadas, S. L., and Nicolls, M. J. (**2012**). "The phases and amplitudes of gravity waves propagating and dissipating in the thermosphere: Theory," J. Geophys. Res. Space Phys. **117**(A5), A05322, https://doi.org/10.1029/2011JA017426.
Vera Rodriguez, I., Nåsholm, S. P., and Le Pichon, A. (**2020**). "Atmospheric wind and temperature profiles inversion using infrasound: An ensemble model context," J. Acoust. Soc. Am. **148**(5), 2923–2934.
Vorobeva, E., Assink, J., Espy, P. J., Renkwitz, T., Chunchuzov, I., and Nåsholm, S. P. (**2023**). "Probing gravity waves in the middle atmosphere using infrasound from explosions," JGR Atmos. **128**(13), e2023JD038725.
Walterscheid, R. L., and Hickey, M. P. (**2001**). "One-gas models with height-dependent mean molecular weight: Effects on gravity wave propagation," J. Geophys. Res. Space Phys. **106**(A12), 28831–28839, https://doi.org/10.1029/2001JA000102.
Walterscheid, R. L., and Hickey, M. P. (**2012**). "Gravity wave propagation in a diffusively separated gas: Effects on the total gas," J. Geophys. Res. Space Phys. **117**(A5), D12101, https://doi.org/10.1029/2011JA017451.
Watson, L. M., Iezzi, A. M., Toney, L., Maher, S. P., Fee, D., McKee, K., Ortiz, H. D., Matoza, R. S., Gestrich, J. E., Bishop, J. W., Witsil, A. J. C., Anderson, J. F., and J. B., Johnson. (**2022**). "Volcano infrasound: Progress and future directions," Bull. Volcanol. **84**(5), 44.
Weaver, A. B., and Alexeenko, A. A. (**2015**). "Revised variable soft sphere and Lennard–Jones model parameters for eight common gases up to 2200 K," J. Phys. Chem. Ref. Data **44**(2), 023103.
Zettergren, M. D., and Snively, J. B. (**2015**). "Ionospheric response to infrasonic-acoustic waves generated by natural hazard events," J. Geophys. Res. Space Phys. **120**(9), 8002–8024, https://doi.org/10.1002/2015ja021116.